Experimental and numerical study on the structural performance of the stainless steel ring strengthened removable dowel bar connection system

Jiachen GUO[1] and Tak-Ming CHAN[1,*]

Department of Civil and Environmental Engineering, The Hong Kong Polytechnic University, Hong Kong, China

* Corresponding author: tak-ming.chan@polyu.edu.hk

Abstract

Traditional jointed plain concrete pavement (JPCP) systems cannot be reused after grouting fast-setting materials in the dowel slot. To achieve demountability, a removable dowel bar connection system is proposed in this paper. The severe stress concentration occurring in JPCP systems is mitigated by applying a stainless steel ring at the pavement joint surface. In the monotonic loading tests, different stainless steel ring thicknesses, lengths and the stainless steel tube thicknesses were considered. The effect of the stainless steel ring on the structural performance of the removable dowel bar connection system was studied in terms of the failure mode, the deflection response, ductility and the strain distribution and development. Besides, after being validated against experimental test results, the developed finite element model was used to conduct the extended parametric analysis, in which a close relationship was found between the ultimate load and the stainless steel ring length. To prevent the localised crushing failure, the maximum compressive stress at the joint surface was compared with the allowable bearing stress under service load. By using FEA data, an empirical equation was finally proposed to predict the ultimate loads of specimens with the proposed connection system.

Keywords: Jointed plain concrete pavement (JPCP), Stress concentration, Demountability, Removable dowel bar connection, Strain development and distribution, Ultimate load.

1. Introduction

Nowadays, well-developed highway systems with high traffic volume gradually call for urgent pavement maintenance and reconstruction since pavements constructed with less durable materials such as asphalt and early-strength concrete are susceptible to damage within 5-10 years (Priddy et al. 2013, Tayabji et al. 2013, Smith and Snyder 2019). To repair damaged pavements, long-time road closures are necessary to ensure concrete to reach a sufficient strength level. It could be deduced that more than 160 billion Euros economic impacts will be caused by traffic congestion by 2025 (Cookson 2016). Besides, the Federal Transit Administration (FTA) within the U.S. Department of Transportation indicated that more than 10 percent traffic jams were attributed to road works (DoT and FHWA 2006). Therefore, fast pavement maintenance and construction techniques become gradually important. Precast concrete pavement (PCP), which allows prefabricated units to be fabricated and assembled off-site, has been developed for nearly 40 years (Tayabji et al. 2013, Smith and Snyder 2019). Once precast elements reach sufficient strength, they will be transported to the construction site and installed on prepared subbases (Olidis et al. 2010, Tayabji et al. 2013, Novak et al. 2017, Smith and Snyder 2019). According to traffic data collected by the Missouri Department of Transportation (DOT), the traffic closure caused user costs have been reduced by 25% after applications of precast concrete pavements (Gopalaratnam et al. 2006). Compared with cast-in-situ concrete pavements, specific benefits of precast concrete pavement (PCP) technology are introduced as follows:

- Better quality and curing condition. Concrete is cast and cured under controlled temperature and moisture. All casting works are carried out by experienced workers with advanced equipment (Tsuji 1996, Merritt and Tayabji 2009, Tayabji et al. 2013, Smith and Snyder 2019, Syed and Sonparote 2020).
- Minimal weather and climate restrictions. Cast-in-situ works cannot be conducted under low temperatures and with rainfalls. However, as prefabricated pavements are manufactured in factories, the effects of temperature and weather are minimised (Tayabji et al. 2013, Novak et al. 2017, Smith and Snyder 2019, Vaitkus et al. 2019).
- Short road closure. Due to no onsite concrete curing, construction and repair works can be started at midnight and finished in the morning (Schexnayder et al. 2007, Chen and Chang 2015, Syed and Sonparote 2017, Vaitkus et al. 2019).
- Higher constructability. Advanced equipment and techniques available in precast concrete pavement (PCP) technology improve construction efficiency (Priddy et al. 2013, Tayabji et al. 2013).
- Higher concrete durability. Precast concrete units are always equipped with extra reinforcements to reduce damages during transportation and installation. Longitudinal and transverse concrete cracks can also be tightened by reinforcements (Priddy et al. 2013, Tayabji et al. 2013, Smith and Snyder 2019).

In the current pavement industry, PCP technology is generally applied in pavement maintenance, reconstruction and new pavement construction (Priddy et al. 2013, Syed and Sonparote 2020). The high durability of precast units makes them more reusable in different applications. Regarding widely used jointed precast concrete pavement (JPrCP) systems, their performances primarily depend on the pavement joint design (Tayabji et al. 2013, Smith and Snyder 2019). To reduce the stress and deflection induced in the loaded pavement slab, epoxy-coated steel dowel bars are commonly used as load transfer devices to transfer a portion of load to the unloaded slab (Murison et al. 2005, Porter and Pierson 2007, Shoukry et al. 2007, Tayabji et al. 2013, Al-Humeidawi and Mandal 2014, El-Maaty et al. 2017, Al-Humeidawi and Mandal 2018, Keymanesh et al. 2018, Smith and Snyder 2019). However, in spite of widespread use for nearly a century (Teller and Cashell 1959), there are still critical issues that deteriorate the joint performance under wheel loads.

- Dowel bar steel corrosion: under fatigue load, thin epoxy coatings are easy to be worn, which then leads to the chloride ion exchange and the corrosion of steel (Shoukry et al. 2002, Murison 2004, Murison et al. 2005, Al-Humeidawi and Mandal 2014, Hu et al. 2017).

- No free movement: steel corrosion and the dowel bar misalignment will create lock-in stress in concrete pavements. Therefore, the free sliding of dowel bars is restricted, resulting in transverse cracks as concrete shrinks due to moisture and temperature changes (Maitra et al. 2009, Tayabji et al. 2013, Smith and Snyder 2019).

- Higher stress concentration: under vertical load, four critical zones form in concrete in the vicinity of the dowel bar. The severe compressive stress concentration at the top and the bottom of the dowel slot will result in the localised concrete crushing (Harrington 2006, Khazanovich et al. 2006, Porter and Pierson 2007, Al-Humeidawi and Mandal 2014, Mackiewicz 2015a). Then the significant tensile stress concentration at two sides of the dowel bar will lead to the initiation of microcracks (Friberg et al. 1939, Shoukry et al. 2002, Riad et al. 2009, Li et al. 2012, Mackiewicz 2015b, Mackiewicz and Szydło 2020).

Figure 1 shows the distributions of compressive and tensile stress within the dowel slot under vertical load. As the stress distribution is symmetric, only half of the tensile stress distribution is plotted.

[Figure 1 near here]To avoid the above-mentioned critical issues, pavement joints should be carefully designed to construct long-life precast concrete pavement systems (Smith and Snyder 2019). To avoid corrosion-related issues, corrosion-free materials such as stainless steel and fibre reinforced polymer (FRP) were suggested to fabricate dowel bars (Eddie et al. 2001, Murison et al. 2005, Khazanovich et al. 2006, Porter and Pierson 2007, Al-Humeidawi and Mandal 2014, Benmokrane et al. 2014). For relieving the severe compressive and tensile stress concentrations, pavement connections must be designed with a large contact area between concrete and steel such as using elliptical and plate dowel bars (Porter and Center 2006, Porter and Pierson 2007, ACPA 2008).

Additionally, demountability is also a potential requirement especially in the design of reusable concrete pavement systems. In traditional JPrCP systems, a fast-setting grouting material is employed to fill the dowel bar slot (Tayabji et al. 2013, Smith and Snyder 2019). Once suffering damages within the service life, the hardened fast-setting material is hard to be removed, which causes difficulties in the pavement slab replacement. Therefore, precast concrete pavement systems should be designed with demountable pavement connections that allow for the flexible installation and replacement of individual pavement slabs.

The objective of the paper is to propose a new removable dowel bar connection system that relieves the severe stress concentration at the joint surface and achieves demountability. Figure 2 introduces the research methodology for the design of the removable dowel bar connection system. The configuration of the removable dowel bar connection is designed to minimise the deficiencies of the traditional dowel bar connection and make full use of the merits of precast concrete pavement technology. Concrete blocks equipped with the removable dowel bar connection are then evaluated experimentally under the monotonic load in terms of the ultimate load and the strain development and distribution. Meanwhile, after being validated against test data, the comprehensive finite element analysis (FEA) is also conducted to further investigate the effects of the stainless steel ring on the ultimate load improvement and the mitigation of stress concentration. According to the test results and the FEA data, an analytical expression in predicting the ultimate load is put forward and the maximum concrete compressive stress at the joint surface is compared with the allowable bearing stress to prevent the localised crushing failure.

[Figure 2 is here]

2. Configuration and materials

2.1. Configuration

The components of the removable dowel bar connection system include the stainless steel dowel bar, the stainless steel tube and the stainless steel ring. The main role of each part is introduced as follows:

- Stainless steel dowel bar: Transfer shear forces between the loaded and the unloaded pavement slabs.
- Stainless steel tube: Create space for the movement of the stainless steel dowel bar and achieve demountability.
- Stainless steel ring: Increase the contact area between concrete and steel to relieve stress concentration and improve the ultimate load.

As corrosion-related issues are severe in the application of traditional epoxy-coated steel dowel bars especially in harsh environments, 304 authentic stainless steel with the high corrosion-resistance ability was used to manufacture each component of the removable pavement connection system. Figure 3(a-d) shows the constitutions of the removable dowel bar connection system. Before concrete casting, the stainless steel tube and the stainless steel ring were welded together and fixed inside the timber formwork by the stainless steel dowel bar at the front and by welded rebars at the end. Specific arrangements of the stainless steel ring and the stainless tube are shown in Figure 3(e,f).

[Figure 3 near here] ***2.2 Material properties***

2.2.1. Concrete

The concrete mixing proportion is shown in Table 1, with the water-cement ratio *w/c* equal to 0.6 and the cement grade CEM I 52.5N. Two types of granite coarse aggregates that had different maximum aggregate sizes were used in the concrete mixing and the geometric property of the fine aggregate followed BS EN 933-1 (2012). The target cylinder compressive strength was 30 MPa to meet the requirement proposed in relevant pavement design codes (AASHTO 1993, Tayabji et al. 2013, Smith and Snyder 2019).

[Table 1 is near here]

Complying with BS EN 12390-3 (2019), BS EN 12390-4 (2019) and BS EN 12390-5 (2019), concrete cylinders and prisms were prepared together with test specimens to evaluate concrete material properties. The workability of the fresh concrete was assessed by implementing the slump test following BS EN 12350-2 (2009). 120 mm slump showed higher workability of the fresh concrete. Relevant material properties of the normal strength concrete are summarised in Table 2.

Figure 4(a) shows the wet concrete after concrete casting. A 4 mm thick plastic sheet was inserted into the slot of the stainless steel tube before concrete casting to create a top slot in the concrete block. The plastic sheet was pulled out after curing for approximately 6 h. Concrete specimens were demoulded after three days and then cured till the test days. The hardened concrete block with a top slot is displayed in Figure 4(b).

[Figure 4 near here]

[Table 2 is near here]

2.2.2. Stainless steel

Two types of coupons were prepared and tested to investigate the material properties of the 304 authentic stainless steel. Curved coupons with a width of 5 mm along the 25 mm gauge length were extracted from stainless steel tubes. The dimensions of the circular coupons milled from the stainless steel dowel bar were determined according to BS EN ISO 6892-1 (2016) and ASTM E8M (2021) with a 10 mm diameter along the 50 mm gauge length.

Tensile coupon tests were conducted using Instron 5982 electro-mechanical high force universal testing system with a capacity of 100 kN. The curved coupon and test setup are shown in Figure 5(a). Two strain gauges attached at both sides of the coupon were used to acquire the modulus of elasticity at the initial stage. The video extensometer at the left side was then used to monitor the change in the distance between two dots and to derive the full-range tensile stress-strain curve. Figure 5(b) shows the circular coupon and the corresponding test arrangement. The stress-strain relationships of stainless steel are plotted in Figure 6. Ductile performance was achieved with elongations of more than 45% at fracture. Specific material properties such as the modulus of elasticity E_s, the yield strength $f_{y(0.2)}$, the ultimate strength f_u as well as the elongation at fracture ε_f are summarised in Table 3. For the stainless steel ring, as it is difficult to manufacture coupons from the ring specimens, the referenced material properties provided by the manufacturer were adopted.

[Figure 5, 6 near here]

[Table 3 is near here]

3. Demountability analysis

Since the main aim of proposing the removable dowel bar connection is to achieve demountability. The individual pavement slab installation and replacement must be achieved. Regarding the installation procedure, firstly, a stainless steel dowel bar is inserted into one pavement slab. Then after placing the other pavement slab in the right location, from the top slot, the installed dowel bar is pushed into the adjacent slab using a long L-shape steel plate. These specific installation procedures are displayed in Figure 7. When the dowel bar moves to the target location, the top slot will be covered with a thin plastic sheet which can also be removed when the pavement slab needs to be replaced.

In terms of the individual pavement slab replacement, firstly removing the thin plastic sheet, then the L-shape steel plate is utilised to push the dowel bar into the adjacent pavement slab. After that, the damaged pavement slab is lifted vertically and replaced with a new one. To clearly describe the removal procedure, Figure 8 is drawn and the detailed layout inside the concrete block is visualised by adjusting the transparency of the concrete block.

[Figure 7, 8 near here]

4. Test methodology

4.1. Test specimens and setup

To evaluate the structural performance of the proposed removable dowel bar connection system, the monotonic loading test was conducted in the Structural Engineering Lab of The

Hong Kong Polytechnic University using a 500 kN hydraulic actuator. The proposed test matrix, including the specimen ID and the dimension of each component, is listed in Table 4.

In the test matrix, both 10- and 20-mm-thick stainless steel rings were included to evaluate the effects of stainless steel ring thickness on the alleviation of the stress concentration and improving the ultimate load. And the length of the stainless steel ring was also studied because the dowel bar deformed nonuniformly within the dowel slot. While the dimension of the stainless steel dowel bar in experiments followed the design guides, with a diameter of 32 mm and a length 460 mm (AASHTO 1993, ACI Committe 325 2002, Tayabji et al. 2013, Smith and Snyder 2019). To consider the installation-related issues, steel tubes may not be laid horizontally before concrete casting. Upward and downward misalignments possibly occurred, as shown in Figure 9. These misalignments could be solved by employing a steel tube with 3 mm thickness and the gap between the dowel bar and the stainless steel tube provided a certain tolerance for the installation. Therefore, structural performances of specimens with the 3 mm-thick stainless steel tube were also tested and compared with standard specimens with the 4 mm-thick tube.

[Figure 9 near here]

[Table 4 is near here]

Research by others indicated that the shear force distribution in dowel bars along the transverse joint followed the linear or parabolic relationship (Friberg et al. 1939, Tabatabaie and Barenberg 1978, Maitra et al. 2009). Transferred shear forces decreased with the increase of the distance from the wheel load. The transverse shear force distribution was also influenced by various parameters including the concrete slab thickness, the concrete compressive strength, the modulus of dowel support, the dowel bar length and spacing, the dowel bar load transfer efficiency, the dowel bar looseness and the pavement support reaction (Guo et al. 1995, Davids et al. 2003, Maitra et al. 2009, Mackiewicz 2015a). Therefore, it was difficult to comprehensively assess all these aspects and the best way to evaluate the dowel bar connection is to focus on the most critical case, namely the maximum load transferred without any damage to an individual connection. Therefore, to determine the critical load, the AASHTO T253 method, proposed by the American Association of State Highway and Transportation Officials (AASHTO 1993), was suggested to test epoxy-coated dowel bars. Since the subbase layer under pavements only affected the load transferred to the adjacent slab while having less effect on the pavement joint performance under wheel load, there was no subbase under the loaded concrete block in the AASHTO T253 method as shown in Figure 10. The load transferred by each dowel bar is equal to half of the applied vertical load. To focus on the shear deformation of the concrete block, the AASHTO T253 method was improved to the modified AASHTO T253 method as shown in Figure 11. The uniformly distributed load was replaced by the concentrated forces at joints and no additional bending deformation was induced in the loaded block, which was more similar to the actual loading condition (Porter and Pierson 2007). However, in these two test methods, an unexpected twisting may occur in the loaded block under vertical load. To solve this issue, the elemental block test was adopted to analyse the individual connection (Li et al. 2012, Al-Humeidawi and Mandal 2014). Figure 12 describes the test setup and the dimension of the concrete specimen was 700 mm × 300 mm × 250 mm. 250 mm was the common thickness of concrete pavements and 300 mm was the same as the dowel bar spacing proposed in design codes (AASHTO 1993, Tayabji et al. 2013, Smith and Snyder 2019). The roller support was located at 100 mm from the concrete block end and the 400 mm × 50 mm × 50 mm rectangular steel block was placed on the top surface of the block and next to the joint surface to exert vertical load. To support the dowel bar outside the concrete block, a vertical abutment was used and tightened to the bottom rigid support by using high-strength bolts. A 13 mm gap was considered between joint surface and the supporting device following the maximum joint width in the jointed concrete pavement design (AASHTO 1993, Tayabji et al. 2013). As the distance between joint and roller support was far larger than that between the loading point and the joint surface, the induced bending deformation in the concrete block could be ignored. The monotonic loading test was carried out with the deflection-controlled loading rate of 0.12 mm per minute. A low loading rate could accurately capture the cracks and crushing initiation and development.

[Figure 10, 11 and 12 near here]

4.2. Data measurement

Under vertical load, the severe stress concentration led to concrete macrocracks and the localised concrete crushing around the dowel bar (Friberg et al. 1939, Heinrichs et al. 1989, Guo et al. 1993, Shoukry et al. 2002, Li et al. 2012, Bronuela et al. 2015, Mackiewicz 2015a).

To evaluate the strain distribution in concrete around the dowel bar, 10 mm strain gauges were mounted along the hoop direction of the pavement connection and vertically along the pavement slab middle line as Figure 13 shows. To assess the stress state far from the connection, 20 mm strain gauges were mounted at 10 mm from the connection side and the distance between 30 mm strain gauges and the pavement connection side was 30 mm. The vertical deformation of the concrete and dowel bar was measured by Linear Variable Displacement Transducers (LVDTs) located at the sides of the concrete block as shown in Figure 14. The vertical deflection of the concrete pavement was determined as the average of side deflections.

[Figure 13, 14 near here]

5. Discussion of results

5.1 Failure modes

With the increase of the vertical load, three different failure modes were observed in experiments: concrete crushing failure, concrete tensile cracks and concrete side shear cracks.

Concrete crushing failure had been pointed out by researchers in previous experimental works (Guo et al. 1993, Eddie et al. 2001, Murison et al. 2005, Porter and Pierson 2007, Li et al. 2012, Al-Humeidawi and Mandal 2014, Benmokrane et al. 2014, Bronuela et al. 2015, Hu et al. 2017, Zuzulova et al. 2020). For each specimen, the localised concrete crushing initially occurred on the top of the pavement connection and then expanded as the load increased. This type of failure was found in each specimen as displayed in Figure 15. Although the concrete crushing failure was severe at the end of the test, it still belonged to a ductile failure as the load drop in specimens failed by concrete crushing such as 32D, 32D3T and 32D3T10R100L was not significant.

[Figure 15 near here]

Horizontal tensile cracks initiated in surrounding concrete around the dowel bar were first mentioned by Friberg et al. (1939). Because of low tensile strength, concrete tensile cracks occurred at both sides of the pavement connection under a small load. With the increase of the vertical load, cracks then propagated horizontally and became macrocracks. As stressed by black lines, Figure 16 captures major tensile cracks generated in specimen 32D and other specimens.

[Figure 16 near here]

Due to the expanded contact area created by the stainless steel ring, the localised crushing zone was enlarged and the ultimate load was thus improved. After reaching the peak load, the expanded crushing zone around the connection impaired the shear resistance of the concrete and then led to the brittle shear failure. Apart from specimens 32D, 32D3T and 32D3T10R100L, other specimens failed suddenly due to the formation of shear cracks at both sides as shown in Figure 17, which initiated on the top surface and then propagated downwards.

[Figure 17 near here]

5.2 Effects of the stainless steel ring on the deflection response

Figure 18 plots the load-deflection relationships of 3T and 4T specimens and the initial stiffness of each specimen is summarized in Table 5. It was found that the specimen with the traditional dowel bar connection had a high initial stiffness because of the direct contact between concrete and steel. While for specimens 32D4T and 32D3T, the small gap between the stainless steel dowel bar and the stainless steel tube reduced the modulus of dowel support and caused a low initial stiffness. However, as the modulus of elasticity of stainless steel was more than six times larger than that of the normal strength concrete, applying the 10- and 20 mm-thick stainless steel rings could improve the initial stiffness. Due to the large gap between the dowel bar and the stainless steel tube, the initial stiffnesses of 3T specimens were lower than those of 4T counterparts in most cases.

As the main role of the stainless steel ring was to expand the contact area between concrete and steel, the effect of the stainless steel ring on the ultimate load was also investigated. The ultimate load of each specimen and the load ratio compared with the traditional dowel bar connection case are summarised in Table 5. For specimen 32D, the maximum load bearing capacity was 126.97 kN. After employing the stainless steel ring, the maximum load bearing capacity of specimens had improved significantly. Equipped with the 10 mm-thick stainless steel ring, the ultimate load was enhanced by more than 40% and up to 100% increment was achieved once strengthened by the 20 mm thick stainless steel ring.

[Figure 18 near here]

[Table 5 is near here]

5.3 Ductility evaluation

To assess the ductility of each specimen, all specimens were divided into two categories. As there was no brittle shear crack found in specimens 32D, 32D3T and 32D3T10R100L at the end of experiments, the load drop within the post-peak stage of the load deflection curve was not obvious, thereby leading to the ductile performance. However, to compare the ductile performance of specimens failed by brittle shear cracks, as defined in Figure 19, the displacement ductility ratio was considered and determined by the deflection at the peak load divided by the yield deflection which was corresponding to the vertical deflection at the intersection of the tangents of the load deflection curve at the initially elastic stage and the horizontal line passing the ultimate load (Park 1989, Azizinamini et al. 1999), where, O is the intersection point; Δ_y and Δ_u are the yield displacement and the displacement at the ultimate load, respectively; N_y and N_u are the yield and the ultimate load, respectively. The yield displacement, the displacement at the ultimate load as well as the displacement ductility ratio for each specimen was listed in Table 6. Compared with specimens with the stainless steel ring of 50 mm length, the longitudianl distribution of the concrete bearing stress was more uniform after applying the 100 mm long stainless steel ring. The development of the concrete crushing zone at the joint surface was thus effectively mitigated.

[Figure 19 near here]

[Table 6 is near here]

5.4 Effects of the stainless steel ring on the strain distribution and development

The strain distribution and development were assessed under service load. For an individual dowel bar, as reported by other researchers, the maximum transferred shear forces ranged from 5.85 kN to 20 kN considering different types of subbase layers (Murison et al. 2005, Maitra et al. 2009, Tayabji et al. 2013, Al-Humeidawi and Mandal 2014, Hu et al. 2017, Mackiewicz and Szydło 2020, Yin et al. 2020, Zuzulova et al. 2020). Similarly, assuming that half of the load was transferred by the dowel bar under the wheel, 20 kN load should be transferred by each dowel bar after considering the 80 kN equivalent single axle load (ESAL) (AASHTO 1993, Tayabji et al. 2013).

5.4.1 Compressive strain

As indicated in the data measurement section, strain gauges CC1-CC3 were attached on the top of the pavement connection to evaluate the compressive strain distribution and development. Under 20 kN service load, the distribution of compressive strain of 4T and 3T specimens is shown in Figure 20. Dash lines indicated the locations of strain gauges CC1, CC2 and CC3 from the edge of the stainless steel ring, respectively. For specimen 32D, the compressive strain measured by CC1 was extremely larger than those measured by CC2 and CC3, resulting in the severe compressive stress concentration at the joint surface under service load. However, after incorporating the stainless steel ring, for both 3T and 4T cases, the compressive stress concentration was effectively relieved as verified by the reduced compressive strain and the linear strain distribution.

[Figure 20 near here]

As for the compressive strain development, owing to the large contact area, the employment of the stainless steel ring could slow down the development of compressive strain. Figure 21 plots the development of the compressive strain evaluated by strain gauge CC1 as the vertical load increased. The rate of the compressive strain development was defined as the slope of the load compressive strain curve determined through the linear regression analysis as summarised in Table 7. It was noted that the rate of compressive strain development of specimen 32D was the highest among all specimens. While after applying the stainless steel ring, the rate of the compressive strain development had been reduced effectively. The relative rate listed in the last column of Table 7 evaluated the strain development rate of each specimen in contrast to specimen 32D. A large relative rate represented the slow development of the compressive strain.

[Figure 21 near here]

[Table 7 is near here]

5.4.2 Tensile strain

Similar to the compressive strain, tensile strains measured in strain gauges could also be used to study the tensile strain distribution and development. 10 mm-strain gauges were adopted to measure the hoop tensile strain and 20 mm and 30 mm-strain gauges to evaluate the horizontal distribution of tensile strain. Table 8 shows the tensile strain measured in each strain gauge and the location of the maximum hoop tensile strain under 20 kN service load. 10 mm, 20 mm as well as 30 mm in the table indicated lengths of strain gauges. It was found that the application of the stainless steel ring played an important role in alleviating the tensile stress concentration. In Figure 22(a), specimen 32D shows a nonlinear tensile strain distribution and the maximum tensile strain concentrated at the sides of the dowel bar is extremely larger than the concrete crack strain. While with the application of the stainless steel ring, from Figure 22(c) to (f), more linear strain distributions were observed and maximum tensile strains were significantly reduced.

[Figure 22 near here]

[Table 8 is near here]

The development of the maximum concrete tensile strain was plotted for each specimen as shown in Figure 23. The maximum tensile strain considered in the tensile strain development was 2000×10^{-6}, twice the tensile strain entering the highly inelastic cracking state (Prabhu et al. 2007). The tensile strain development before 2000×10^{-6} could be briefly divided into two stages. The first stage was the uncracked stage with no microcracks initiation and a lower rate of tensile strain development. The second stage referred to the strain development stage. Within this stage, some microcracks initiated and then gradually propagated. For specimen 32D, the uncracked stage could be ignored and microcracks initiated under a low load. However, after employing the stainless steel ring, the uncrack stage became obvious and thus fewer microcracks appeared under service load. Therefore, the stainless steel ring was suggested to be adopted to alleviate the propagation of microcracks.

[Figure 23 near here]

In this section, the effect of the stainless steel ring on strengthening the removable dowel bar connection was studied from the compressive and tensile strain perspectives. It was concluded that the stainless steel ring had a significant impact on relieving stress concentration and creating a linear strain distribution under service load.

6. Finite element analysis

Apart from experiments, FEA was also conducted using the commercial finite element analysis software ABAQUS to further investigate the structural performance of the stainless steel ring strengthened removable dowel bar connection system (ABAQUS 6.14 2014). As the gap between the stainless steel dowel bar and the stainless steel tube may induce convergence issues, all models were developed with the 4 mm thick stainless steel tube to eliminate gaps.

6.1 Finite element model

The configuration of the finite element model followed the actual specimen dimension in the tests. Each part of the model was simulated with three-dimensional solid elements with reduced integration (C3D8R). Figure 24 shows each component and the whole model after assembly. The interaction between each part was simulated by the surface-to-surface contact with the normal behaviour modelled by the 'hard contact' without penetration allowed. The tangential behaviour was modelled by the 'penalty' friction formulation with a specific frictional coefficient. According to the FEA conducted by Al-Humeidawi and Mandal et al. (2022), the friction coefficient between steel and concrete was 0.35. Then to simulate the tangential contact behaviour between lubricated steel surfaces, the corresponding friction coefficient was adjusted to 0.15 as recommended by Velkavrh et al. (2011) and Pijpers et al. (2020).

[Figure 24 near here]

The boundary conditions of the finite element model followed the real test setting. To simplify the model and avoid convergence issues, the roller support in the FE model was replaced by the coupling constraint to the reference point RP-1 as shown in Figure 25(a). The displacement along Y axis U2, along Z axis U3, and the rotation about X axis UR1 as well as about Z axis UR3 were restricted. For the fixing device, all degrees of freedom of the bottom surface were constrained as displayed in Figure 25(b). As shown in Figure 25(c), the displacement-controlled vertical load was exerted to the loading block by the coupling constraint to the reference point RP-2.

[Figure 25 near here]

6.2 Concrete material modeling

The concrete damaged plasticity (CDP) model, proposed by Lubliner et al (1989) and modified by Lee and Fenves (1998), available in ABAQUS was used to simulate the complex behaviour of concrete. In the CDP model, the behaviour of concrete under uniaxial compression and tension was firstly defined. The uniaxial compressive stress-strain relationship of concrete could be divided into two stages, namely the linear elastic stage and the nonlinear plastic stage. For the linear elastic stage, before $0.4f_c$, compressive stress increased proportionally to the compressive strain, where f_c is the cylinder compressive strength of concrete. The corresponding secant modulus of elasticity E_c, determined from the origin to $0.4f_c$, was regarded as the modulus of elasticity of concrete in the CDP model. In terms of the nonlinear plastic stage, Equations (1)-(3) proposed in CEB-FIP Model Code 2010 were adopted (CEB-FIP 2010), where, σ_c is the concrete compressive stress; ε_c is the compressive strain; ε_{cl} is the compressive strain at the cylinder compressive strength; E_{ci} is the tangential modulus of elasticity of concrete at the origin; E_{cl} is the secant modulus of elasticity of concrete from the origin to the compressive strength; k is the plasticity number. The limited compressive strain $\varepsilon_{c,lim}$ was the strain at $0.5f_c$ within the post peak stage. For the descending stage beyond the limited strain, Equations (4) and (5) suggested in CEB-FIP Model Code 1990 were used (CEB-FIP 1993). All material parameters related to concrete under the uniaxial compression are summarised in Table 9 and the full stress-strain curve is described in Figure 26.

$$\frac{\sigma_c}{f_c} = \left[\frac{k\eta - \eta^2}{1 + (k-2)\eta}\right] \; for \; \varepsilon_c < \varepsilon_{c,lim} \tag{1}$$

$$\eta = \left(\frac{\varepsilon_c}{\varepsilon_{cl}}\right) \tag{2}$$

$$k = \left(\frac{E_{ci}}{E_{cl}}\right) \tag{3}$$

$$\sigma_c = \left[\left(\frac{1}{\frac{\varepsilon_{c,lim}}{\varepsilon_{cl}}}\xi - \frac{2}{\left(\frac{\varepsilon_{c,lim}}{\varepsilon_{cl}}\right)^2}\right)\left(\frac{\varepsilon_c}{\varepsilon_{cl}}\right)^2 + \left(\frac{4}{\frac{\varepsilon_{c,lim}}{\varepsilon_{cl}}} - \xi\right)\left(\frac{\varepsilon_c}{\varepsilon_{cl}}\right)\right]^{-1} f_c \tag{4}$$

$$\xi = \frac{4\left[\left(\frac{\varepsilon_{c,lim}}{\varepsilon_{cl}}\right)^2\left(\frac{E_{ci}}{E_{cl}} - 2\right) + 2\frac{\varepsilon_{c,lim}}{\varepsilon_{cl}} - \frac{E_{ci}}{E_{cl}}\right]}{\left[\frac{\varepsilon_{c,lim}}{\varepsilon_{cl}}\left(\frac{E_{ci}}{E_{cl}} - 2\right) + 1\right]^2} \tag{5}$$

[Figure 26 near here]

[Table 9 is near here]

In terms of the uniaxial tensile behaviour of concrete, the stress-crack width independent of the mesh size was suggested. Before reaching the uniaxial tensile strength, the linear elastic behaviour was defined. Regarding the descending stage, the bilinear stress versus crack width relationship in CEB-FIP Model Code 2010 was used as expressed from Equations (6) to (10) (CEB-FIP 2010), where, f_t is the uniaxial tensile strength of concrete; σ_{ct} is the concrete tensile stress; w is the crack width; w_t is the transition crack width; w_c is the crack opening width. Table 10 lists the material properties of concrete under uniaxial tension and the bilinear stress-crack width curve in the CDP model is depicted in Figure 27.

$$\sigma_{\mathrm{ct}} = f_{\mathrm{t}}\left(1.0 - 0.8\frac{w}{w_1}\right)\ for\ w \leq w_{\mathrm{t}} \tag{6}$$

$$\sigma_{\mathrm{ct}} = f_{\mathrm{t}}\left(0.25 - 0.05\frac{w}{w_1}\right)\ for\ w_{\mathrm{t}} < w \leq w_{\mathrm{c}} \tag{7}$$

$$G_{\mathrm{F}} = 0.73 f_{\mathrm{c}}^{0.18} \tag{8}$$

$$w_{\mathrm{t}} = \frac{G_{\mathrm{F}}}{f_{\mathrm{t}}} \tag{9}$$

$$w_{\mathrm{c}} = \frac{5G_{\mathrm{F}}}{f_{\mathrm{t}}} \tag{10}$$

[Figure 27 near here]

[Table 10 is near here]

Concrete compressive and tensile damage variables d_c and d_t were also incorporated in FEA to consider the effect of the concrete crushing and micro-cracks on the reduced stiffness. Assuming that the concrete compressive damage is accumulated with the concrete plastic strain $\varepsilon_{\mathrm{c}}^{\mathrm{pl}}$, the compressive damage variable d_c is determined by Equation (11) as shown in Figure 28 (Birtel and Mark 2006). For concrete tensile damage, defined by the dissipated energy to form the microcrack, the concrete tensile damage variable d_t in the CDP model is calculated by Equations (12) and (13), which is related to the crack width w, the transition crack width w_t, the crack opening width w_c, the uniaxial tensile strength of concrete f_t as well as the fracture energy G_F. The evolution of concrete tensile damage variable d_t with the increase of the crack width is plotted in Figure 29.

$$d_c = 1 - \frac{\sigma_c E_c^{-1}}{\varepsilon_c^{pl}\left(\frac{1}{b_c} - 1\right) + \sigma_c E_c^{-1}}, b_c = 0.7 \tag{11}$$

$$d_t = \frac{f_t\left(w - 0.4\frac{w^2}{w_t}\right)}{G_F}, w \leq w_t \tag{12}$$

$$d_t = \frac{\left[f_t\left(0.125 - 0.025\frac{w}{w_t}\right)(w_c - w)\right]}{G_F}, w_t < w \leq w_c \tag{13}$$

Other parameters in the CDP model including the dilation angle ψ, the biaxial compressive strength ratio σ_{b0}/f_{c0}, the ratio of the tensile-to-compressive meridian K, eccentricity ϵ and the viscosity parameter were determined according to the ABAQUS user guide (2014), equal to 38°, 1.16, 0.667, 0.1 and zero, respectively.

[Figure 28, 29 near here]

6.3 Stainless steel material modelling

The nonlinear stress-strain behaviour of stainless steel was modelled using the stress-strain curves obtained from the coupon tests as plotted in Figure 6. The true stress-strain relationship was transferred from the nominal stress-strain curve with the converted expressions as indicated in Equations (14) and (15). The stainless steel ring was treated as the elastic part with a modulus of elasticity of 190 GPa.

$$\sigma_{\mathrm{t}} = \sigma(1+\varepsilon) \tag{14}$$

$$\varepsilon_{\mathrm{t}} = ln(1+\varepsilon) \tag{15}$$

6.4 Model validation

Through mesh convergence analysis, the predicted ultimate load performed a convergent trend when the mesh size of the localised region around the connection was 4 mm. As the typical concrete crushing failure primarily occurred near the joint surface, to minimise computational efforts, the global mesh size of 15 mm was applied in regions far from the pavement joint. The finite element model was then validated against test data in terms of the failure mode and the load-deflection curve. As shown in Figure 30(a), the severe concrete crushing failure was displayed by the concrete compressive damage variable d_c in models 32D, 32D4T and 32D4T10R100L as stressed in localised red zones. The particular shear crack failure in specimen 32D4T10R100L was also well simulated by the concrete tensile damage variable d_t as described in Figure 30(b). Regarding the load-deflection relationship, the deflection responses of model 32D and 32D4T could be well predicted in FEA as plotted in Figure 30(c). Due to the elimination of gaps between different components in FEA, the stiffness of model 32D4T10R100L was overestimated. However, the high stiffness had a limited impact on the ultimate limit state (ULS). As depicted in Figure 31 and summarised in Table 11, the differences between the FE predictions and the test results were lower than 10% in terms of the ultimate load.

[Figure 30, 31 near here]

[Table 11 is near here]

6.5 Effect of the stainless steel ring on the ultimate load

To further study the effect of the stainless steel ring on the ultimate load, models with the stainless steel ring of thickness ranging from 5 mm to 25 mm and the length ranging from 25 mm to 150 mm were developed. The ultimate load of each specimen is summarised in Table 12 and plotted in Figure 32. With the increase of the stainless steel ring thickness, the contact area between steel and concrete was expanded. Therefore, the bearing resistance of concrete and the ultimate load of the model had been improved. Moreover, under vertical load, the distribution of bearing stress along the dowel bar was more uniform when a longer stainless steel ring is applied. From the dash lines depicted in Figure 32, with a high coefficient of determinations (R^2), the ultimate load increased almost linearly with the stainless steel ring length.

[Figure 32 near here]

[Table 12 is near here]

6.6 Effect of the stainless steel ring on the maximum compressive stress

Since the compressive stress was concentrated at a localised zone around the pavement connection, it is hard to determine the maximum compressive stress experimentally. Accordingly, the normal contact stress of each specimen, which is equal to the maximum compressive stress at the joint surface, was obtained in FEA and plotted in Figure 33. Although prolonging the length of the stainless steel ring also reduced the normal contact stress, this effect was less significant than increasing the stainless steel ring thickness. As concrete pavement systems are under cyclic wheel loads in practice, it is necessary to analyse the maximum compressive stress from the fatigue perspective. Generally, the newly constructed concrete pavement is suggested to be designed with 40 years of service life (Tayabji et al. 2013, Smith et al. 2014, Smith and Snyder 2019). Within this period, concrete pavement systems should be designed to bear 10^6-10^8 cycles of repetitive wheel loads without any damage (Lee and Barr 2004, Tayabji et al. 2013, Smith and Snyder 2019). The load transfer efficiency refers to the ability to transfer the applied load from the loaded slab to the unloaded slab, which closely depends on the relative deflection between adjacent slabs. Under fatigue loads, the concentrated compressive stress at the joint surface will induce the localised concrete crushing around the pavement connection and thus cause the reductions of joint stiffness and load transfer efficiency (Harrington 2006, Khazanovich et al. 2006, Porter and Pierson 2007, Al-Humeidawi and Mandal 2014). As a result, to protect the concrete pavement systems from the localised crushing failure, the allowable bearing stress under fatigue loads was calculated.

[Figure 33 near here]

According to American Concrete Institute (ACI) subcommittee 325 (1956), the allowable bearing stress in concrete is determined according to Equation (16). Where f_b is the allowable bearing stress and d is the dowel bar diameter. Considering the dowel bar of 32 mm diameter, the allowable bearing stress is 29.15 MPa with a concrete compressive strength of 31.92 MPa.

$$f_b = f_c(4 - d/25.4)/3 \quad (16)$$

However, this allowable bearing stress is independent of the number of loading cycles and the concrete age. Therefore, the reliability of this allowable stress should be further assessed. Equations (17) and (18) proposed in CEB-FIP Model Code 2010 were adopted to calculate the fatigue compressive strength considering the concrete age (CEB-FIP 2010), where, $\beta_{cc}(t)f_{ck}$ is the concrete compressive strength at various ages; $s=0.2$ when CEN 52.5 N cement is used; $\beta_{c,sus}(t, t_0)$ is taken as 0.85 for the fatigue loading. As a result, the fatigue compressive strength after 40 years calculated by Equations (17) and (18) was 30.30 MPa. Then the typical S-N relationship proposed in CEB-FIP Model Code 2010 was used to calculate the allowable bearing stress under different loading cycles as expressed in Equations (19)-(23), where, N is the total number of loading cycles; $S_{c,max}$ and $S_{c,min}$ are the maximum and minimum compressive stress ratios under cyclic loads calculated by Equations (22) and (23), respectively. This relationship was plotted as the typical S-N curves as shown in Figure 33. When $S_{c,min}$ is equal to zero, the maximum allowable bearing stress determined by Equation (19) was from 13.64 MPa to 17.80 MPa with loading cycles from 10^6 to 10^8. The normal contact stress at the joint surface was then compared with the allowable bearing stress. According to ACI subcommittee 325, apart from specimens 32D and 32D4T, other specimens could meet the bearing stress requirement under 20 kN service load. However, after considering the number of loading cycles and the concrete age by Equations (17) to (23), employing the stainless steel ring with at least 15 mm thickness could meet the fatigue requirement under cyclic loads.

$$f_{\mathrm{ck,fat}} = \beta_{\mathrm{cc}}(t) f_{\mathrm{ck}} \beta_{\mathrm{c,sus}}(t, t_0)\left(1 - \frac{f_{\mathrm{ck}}}{400}\right) \tag{17}$$

$$\beta_{\mathrm{cc}}(t) = exp\left\{s\left[1 - \left(\frac{28}{t}\right)^{0.5}\right]\right\} \tag{18}$$

$$log\, N = \frac{8}{(Y-1)}\left(S_{\mathrm{c,max}} - 1\right)\,(logN \le 8) \tag{19}$$

$$log\, N = 8 + \frac{8\ln(10)}{(Y-1)}\left(Y - S_{\mathrm{c,min}}\right) log\left(\frac{S_{\mathrm{c,max}} - S_{\mathrm{c,min}}}{Y - S_{\mathrm{c,min}}}\right)(logN > 8) \tag{20}$$

$$Y = \frac{0.45 + 1.8S_{\mathrm{c,min}}}{1 + 1.8S_{\mathrm{c,min}} - 0.3S_{\mathrm{c,min}}^2} \tag{21}$$

$$S_{\mathrm{c,max}} = \left|\sigma_{\mathrm{c,max}}\right| / f_{\mathrm{ck,fat}} \tag{22}$$

$$S_{\mathrm{c,min}} = \left|\sigma_{\mathrm{c,min}}\right| / f_{\mathrm{ck,fat}} \tag{23}$$

[Figure 34 near here]

7. Design recommendation

According to the test data and the FEA results, the stainless steel ring strengthened removable dowel bar connection should be designed from two aspects including the design for the ultimate load and the design for the service load. Considering the stainless steel ring thickness and length, the following Equation (24) is proposed to predict the ultimate load, where N_u is the ultimate load, t is the stainless steel ring thickness and l is the stainless steel ring length. Constant 157.4 in Equation (24) is the peak load of specimen 32D4T predicted in FEA.

$$N_u = (0.0134t + 0.043)l + 0.0394t^2 + 0.905t + 157.4 \tag{24}$$

In terms of the design under 20 kN service load, taking into account the total loading cycles within the pavement service life, the allowable bearing stress is calculated based on the typical S-N relationship of concrete under compression. After comparing the allowable bearing stress with the normal contact stress acquired from FEA, at least the 15 mm thick stainless steel ring is suggested to be adopted in the design of the removable dowel bar connection system.

8. Conclusions

This paper introduces an innovative removable dowel bar connection system that achieves the reusability of the individual pavement unit and ensures effective load transfer. To address severe stress concentration occurring in the traditional dowel bar application, an additional stainless steel ring was incorporated and placed at the joint surface. In experiments, specimens with the removable dowel bar connection were evaluated in terms of the failure mode, the deflection response, ductility and the concrete strain distribution and development. Through FEA, the effects of the stainless steel ring on the ultimate load improvement and the mitigation of the compressive stress concentration were also comprehensively investigated. According to test data and FEA results, the following conclusions are drawn:

(1) Specimen with the traditional dowel bar connection suffered severe compressive and tensile stress concentration at the joint surface. The localised concrete crushing and horizontal tensile cracks significantly developed under service load.

(2) The gap between the stainless steel dowel bar and the stainless steel tube not only provides tolerances for installation but also improves the ductility of the specimen with the removable dowel bar connection.

(3) Applying the stainless steel ring improves the bearing resistance of the surrounding concrete. Therefore, the ultimate load of the specimen enhances as the thickness of the stainless steel ring increases.

(4) Based on test results and FEA data, a close linear relationship is observed between the ultimate load and the length of the stainless steel ring.

(5) The contact area between steel and concrete is expanded with the application of the stainless steel ring. Therefore, under service load, the maximum concrete compressive stress at the joint surface is reduced and the compressive stress concentration is alleviated.

(6) Under service load, the strain localisation observed in the specimen with the traditional dowel bar connection is considerably improved after applying the stainless steel ring. A linear strain distribution of concrete is achieved around the removable dowel bar connection.

Based on test results and FEA data, an empirical equation to predict the ultimate load of the specimen with the removable dowel bar connection is proposed. Under 20 kN service load, the stainless steel ring with at least 15 mm thickness should be employed to avoid the localised crushing failure within the pavement service life.

Acknowledgements

The research work presented in this paper was supported by a grant from the Research Grants Council of the Hong Kong Special Administrative Region, China (Project no. R5007-18). The authors would like to sincerely acknowledge the advice on the joint design from Professor Yuhong Wang at The Hong Kong Polytechnic University. The authors would also like to thank the technical staff, Mr. H.Y. Leung and Mr. K.H. Wong of the Structural Engineering Research Laboratory and Concrete Technology laboratory for their support as well as the support from the Industrial Centre at The Hong Kong Polytechnic University.

Disclosure statement

No potential conflict of interest was reported by the author(s).

Funding

This work was supported by Research Grants Council, University Grants Committee [Grant number R5007-18].

References

American Association of State Highway and Transportation Officials, 1993. Guide for design of pavement structure. Washington D.C: AASHTO.

ABAQUS 6.14, 2014. Dassault systems, Waltham, MA, USA.

ABAQUS. 6.14 CAE User’s Guide, 2014. Dassault systems, Waltham, MA, USA.

ACI Committee 325, 1956. Structural design considerations for pavement joints. *Journal of the American Concrete Institute.* 1-28.

ACI Committee 325, 2002. ACI 325.12R-02 Guide for design of jointed concrete pavements for streets and local roads. American Concrete Institute, Detroit, MI.

Al-Humeidawi, B. H. and Mandal, P. 2014. Evaluation of performance and design of GFRP dowels in jointed plain concrete pavement–part 1: experimental investigation. *International Journal of Pavement Engineering,* 15(5), 449-459.

Al-Humeidawi, B. H. and Mandal, P. 2018. Experimental investigation on the combined effect of dowel misalignment and cyclic wheel loading on dowel bar performance in JPCP. *Engineering Structures,* 174, 256-266.

Al-Humeidawi, B. H. and Mandal, P. 2022. Numerical evaluation of the combined effect of dowel misalignment and wheel load on dowel bars performance in JPCP. *Engineering Structures,* 252, 113655.

American College Personnel Association, 2008. An Alternative to Traditional Round Dowel Bars.

ASTM E8 / E8M, 2021. Standard Test Methods for Tension Testing of Metallic

Materials. American Society for Testing and Materials.

Azizinamini, A., *et al.*, 1999. Proposed modifications to ACI 318-95 tension development and lap splice for high-strength concrete.

Benmokrane, B., et al., 2014. Performance of glass fiber-reinforced polymer-doweled jointed plain concrete pavement under static and cyclic loadings. Aci Structural Journal, 111 (2), 331–342.

Birtel, V. and Mark, P., 2006. Parameterised finite element modelling of RC beam shear failure. ed. *ABAQUS users' conference*.

Bronuela, L., Ryu, S. and Cho, Y. H., 2015. Cantilever and pull-out tests and corresponding FEM models of various dowel bars in airport concrete pavement. *Construction Building Materials,* 83, 181-188.

BS EN 12350-2, 2009. Testing hardened concrete-Part 2: Slump test.

BS EN 933-1, 2012. Tests for geometrical properties of aggregates.

BS EN ISO 6982-1, 2016. Metallic materials-Tensile testing-Part 1: Method of test at room temperature.

BS EN 12390-3, 2019. Testing hardened concrete-Part 3: Compressive strength of test specimens.

BS EN 12390-4, 2019. Testing Hardened Concrete-Part 4: Compressive Strength. Specification for Testing Machines.

BS EN 12390-5, 2019. Testing hardened concrete-Part 5: Flexural strength of test specimens.

CEB/FIP, 1993. CEB-FIP model code 1990: Design code.Switzerland: Thomas Telford Publishing.

CEB/FIP, 2010. Model code for concrete structures. Berlin, Germany:Ernst & Sohn, Wiley.

Chen, Y.-T. and Chang, L.-M., 2015. Paving for the future-Precast Prestressed Concrete Pavement (PPCP). *Scientific Cooperations Journal of Civil Engineering Architecture,* 1(1), 7-12.

Cookson, G., 2016. Europes Traffic Hotspots Measuring the impact of congestion. *INRIX research*.

Davids, W. G*., et al.*, 2003. Three-dimensional finite element analysis of jointed plain concrete pavement with EverFE2. 2. *Transportation Research Record,* 1853(1), 92-99.

U.S. Department of Transportation., 2006. Status of the Nation's Highways, Bridges, and Transit: Conditions and Performance. *Report to Congress*.

Eddie, D., Shalaby, A. and Rizkalla, S., 2001. Glass fiber-reinforced polymer dowels for concrete pavements. *Aci Structural Journal,* 98(2), 201-206.

El-Maaty, A. E. A*., et al.*, 2017. Characteristics of Jointed Rigid Airfield Pavement Using Different Material Parameters and Modeling Techniques. ed. *International Congress and Exhibition "Sustainable Civil Infrastructures: Innovative Infrastructure Geotechnology"*, 66-84.

Friberg, B., Richart, F. and Bradbury, R., 1939. Load and deflection characteristics of dowels in transverse joints of concrete pavements. ed. *Highway Research Board Proceedings*.

Gopalaratnam, V. S*., et al.*, 2006. Precast Prestressed Panels for Rapid Full-Depth Pavement Repairs. ed. *Structures Congress 2006: Structural Engineering and Public Safety*, 1-10.

Guo, H., Pasko, T. and Snyder, M., 1993. Maximum bearing stress of concrete in doweled portland cement concrete pavements. *Transportation Research Record,* 1388, 19.

Guo, H., Sherwood, J. A. and Snyder, M. B., 1995. Component dowel-bar model for load-transfer systems in PCC pavements. *Journal of Transportation Engineering,* 121(3), 289-298.

Harrington, J. F., 2006. Comparison of alternative laboratory dowel bar testing procedures.

Heinrichs, K. W, et al., 1989. Rigid pavement analysis and design. United States: Federal Highway Administration.

Hu, CC., et al., 2017.Experimental study of dowel bar alternatives based on similarity model test. Advances in Materials Science Engineering, 2017, 1–9.

Keymanesh, M*., et al.*, 2018. Evaluating the Performance of Dowel in PCC Pavement of Roads using ABAQUS Finite Element Software. *International Journal of Transportation Engineering,* 5(4), 349-365.

Khazanovich, L*., et al.*, 2006. Accelerated loading testing of stainless steel hollow tube dowels. *Transportation Research Record,* 1947(1), 101-109.

Lee, J. and Fenves, G. L., 1998. Plastic-damage model for cyclic loading of concrete structures. *Journal of Engineering Mechanics,* 124(8), 892-900.

Lee, M. and Barr, B., 2004. An overview of the fatigue behaviour of plain and fibre reinforced concrete. *Cement Concrete Composites,* 26(4), 299-305.

Lubliner, J.*, et al.*, 1989. A plastic-damage model for concrete. *International Journal of solids structures,* 25(3), 299-326.

Li LK*., et al.*, 2012. Characterization of Contact Stresses Between Dowels and Surrounding Concrete in Jointed Concrete Pavement.

Mackiewicz, P., 2015a. Analysis of stresses in concrete pavement under a dowel according to its diameter and load transfer efficiency. *Canadian Journal of Civil Engineering,* 42(11), 845-853.

Mackiewicz, P., 2015b. Finite-element analysis of stress concentration around dowel bars in jointed plain concrete pavement. *Journal of Transportation Engineering,* 141(6), 06015001.

Mackiewicz, P. and Szydło, A., 2020. The analysis of stress concentration around dowel bars in concrete pavement. *Magazine of Concrete Research,* 72(2), 97-107.

Maitra, S. R., Reddy, K. and Ramachandra, L., 2009. Load transfer characteristics of dowel bar system in jointed concrete pavement. *International Journal of Fracture,* 135(11), 813-821.

Merritt, D. K. and Tayabji, S., 2009. Precast Prestressed Concrete Pavement for

Reconstruction and Rehabilitation of Existing Pavements.

Murison, S., 2004. Evaluation of concrete-filled GFRP dowels for jointed concrete pavements.

Murison, S., Shalaby, A. and Mufti, A., 2005. Concrete-Filled, Glass Fiber–Reinforced Polymer Dowels for Load Transfer in Jointed Rigid Pavements. *Transportation Research Record,* 1919(1), 54-64.

Novak, J., *et al.*, 2017. Precast concrete pavement–systems and performance review. *IOP Conference Series: Materials Science and Engineering*, 012030.

Olidis, C., *et al.*, 2010. Precast Slab Literature Review Report: Repair of Rigid Airfield Pavements Using Precast Concrete Panels-A State-of-the-Art Review.

Park, R., 1989. Evaluation of ductility of structures and structural assemblages from laboratory testing. *Bulletin of the New Zealand Society for Earthquake Engineering,* 22(3), 155-166.

Pijpers R, Slot H., 2020. Friction coefficients for steel to steel contact surfaces in air and seawater. *Journal of Physics: Conference Series*, 012002.

Porter, M. and Pierson, N., 2007. Laboratory evaluation of alternative dowel bars for use in Portland cement concrete pavement construction. *Transportation Research Record,* 2040(1), 80-87.

Porter, M. L. and Center, C. T., 2006. testing structural Behavior of alternative Dowel Bars.

Prabhu, M., Varma, A. H. and Buch, N., 2007. Experimental and analytical investigations of mechanistic effects of dowel misalignment in jointed concrete pavements. *Transportation Research Record,* 2037(1), 12-29.

Priddy, L. P., Bly, P. G. and Flintsch, G. W., 2013. Review of precast portland cement concrete panel technologies for use in expedient portland cement concrete airfield pavement repairs.

Riad, M. Y., *et al.*, 2009. Effect of skewed joints on the performance of jointed concrete pavement through 3D dynamic finite element analysis. *International Journal of Pavement Engineering,* 10(4), 251-263.

Schexnayder, C., Ullman, G. and Anderson, S., 2007. Pavement reconstruction scenarios using precast concrete pavement panels. *Practice Periodical on Structural Design,* 12(4), 186-199.

Shoukry, S., William, G. and Riad, M., 2007. Effect of thermal stresses on mid-slab cracking in dowel jointed concrete pavements. *Structure Infrastructure Engineering,* 3(1), 43-51.

Shoukry, S. N., William, G. and Riad, M., 2002. Characteristics of concrete contact stresses in doweled transverse joints. *International Journal of Pavement Engineering,* 3(2), 117-129.

Smith, K. D, et al., 2014. Concrete pavement preservation guide. U.S. Department of Transportation: Federal Highway Administration.

Smith, P. and Snyder, M. B., 2019. *Manual for Jointed Precast Concrete Pavement.* National Precast Concrete Association.

Syed, A. and Sonparote, R., 2017. Analysis of prestressed precast concrete pavement. *Materials Today: Proceedings,* 4(9), 9713-9717.

Syed, A. and Sonparote, R., 2020. A review of precast concrete pavement technology. *Baltic Journal of Road Bridge Engineering,* 15(4).

Tabatabaie, A. M., and Barenberg,E, 1978. Finite-element analysis of jointed or cracked concrete pavements.Transportation Research Record, 671, 11–19.

Tayabji, S., Ye, D., and Buch, N, 2013. Precast concrete pavement technology. Washington:Transportation Research Board.

Teller, L. W., and Cashell, H. D, 1959. Performance of doweled joints under repetitive loading. Highway Research Board Bulletin, 217, 8–49.

Tsuji, T., 1996. Joint structure for coupling precast concrete pavement slabs. Google Patents.

Vaitkus, A.*, et al.*, 2019. Concrete modular pavements–types, issues and challenges. *The Baltic Journal of Road Bridge Engineering,* 14(1), 80-103.

Velkavrh I, Kalin M., 2011. Effect of base oil lubrication in comparison with non-lubricated sliding in diamond-like carbon contacts. *Tribology-Materials, Surfaces & Interfaces,* 5:53-58.

Yin, W., et al., 2020. Mechanical characteristics of dowel bar-concrete interaction: based on substructure experiment. International Journal of Pavement Engineering, 23 (7), 1–13.

Zuzulova, A., Grosek, J. and Janku, M., 2020. Experimental laboratory testing on behavior of dowels in concrete pavements. *Materials,* 13(10), 2343.

Table 1 Normal strength concrete mixing proportion (kg/m^3).

Water	Cement	Sand	Aggregate	
			20mm	10mm
185	308	667	831	410

Table 2 Material properties of normal strength concrete (MPa).

Compressive strength	Splitting tensile strength	Flexural strength
31.92	2.98	4.79

Table 3 Material properties of 304 authentic stainless steel.

Stainless steel	Modulus of elasticity E_s (GPa)	Yield strength $f_{y(0.2)}$ (MPa)	Ultimate strength f_u (MPa)	Elongation ε_f (%)
Dowel bar	190.3	327.7	748.0	47
4 mm tube	190.2	269.1	729.0	57
3 mm tube	193.2	283.4	757.0	55
Steel ring	190.0	260.0	650.0	43

Table 4 Test matrix for the removable dowel bar connection.

Specimen ID	Dowel bar	Stainless steel tube		Stainless steel ring		
	Dowel bar diameter (mm)	Tube external diameter (mm)	Tube internal diameter (mm)	Ring external diameter (mm)	Ring internal diameter (mm)	Ring length (mm)
32D	31.97					
32D3T	31.97	40.15	33.89			
32D3T10R50L	31.97	40.20	33.84	60.41	40.47	51.65
32D3T10R100L	31.97	40.13	33.87	60.42	40.79	106.61
32D3T20R50L	31.97	40.21	33.79	80.01	40.39	50.97
32D3T20R100L	31.97	40.26	33.89	79.99	40.47	101.34
32D4T	31.97	40.17	32.21			
32D4T10R50L	31.97	39.86	32.19	60.34	40.17	51.12
32D4T10R100L	31.97	40.20	32.16	60.45	40.69	107.58
32D4T20R50L	31.97	39.91	32.18	80.46	40.10	52.02
32D4T20R100L	31.97	39.79	32.19	80.33	40.28	101.61

32D is the 32 mm-diameter stainless steel dowel bar;

3T and 4T refer to the 3 mm and 4 mm-thick stainless steel tubes, respectively;

10R and 20R denote the 10 mm and 20 mm-thick stainless steel rings, respectively;

50L and 100L mean the stainless steel rings with 50 mm and 100 mm length, respectively.

Table 5 Initial stiffness and ultimate load (kN).

Specimen ID	Initial stiffness (kN/mm)	Ultimate load (kN)	Load ratio
32D	106.7	126.97	1
32D4T	89.7	166.29	1.31
32D4T10R50L	102.2	183.68	1.45
32D4T10R100L	112.8	185.55	1.46
32D4T20R50L	118.6	195.71	1.54
32D4T20R100L	125.3	232.59	1.83
32D3T	77.4	167.14	1.32
32D3T10R50L	89.8	192.42	1.52
32D3T10R100L	97.7	195.09	1.54
32D3T20R50L	121.8	205.30	1.62
32D3T20R100L	119.5	261.09	2.06

Table 6 Displacement ductility ratio.

Specimen type	Yield deflection Δ_y (mm)	Peak load deflection Δ_u (mm)	Displacement ductility ratio
32D	1.19	3.04	2.55
32D4T	1.85	5.88	3.18
32D4T10R50L	1.80	4.01	2.23
32D4T10R100L	1.64	4.68	2.85
32D4T20R50L	1.65	4.29	2.60
32D4T20R100L	1.86	5.80	3.12
32D3T	2.16	5.43	2.51
32D3T10R50L	2.14	4.80	2.24
32D3T10R100L	2.00	4.77	2.39
32D3T20R50L	1.69	5.00	2.96
32D3T20R100L	2.18	10.07	4.62

Table 7 The rate of compressive strain development.

Specimen type	The compressive strain development rate ($\times 10^6$ kN)	Relative rate
32D	-0.0105	1.00
32D4T	-0.0191	1.82
32D4T10R50L	-0.0262	2.50
32D4T10R100L	-0.0337	3.21
32D4T20R50L	-0.0680	6.48
32D4T20R100L	-0.0747	7.11
32D3T	-0.0144	1.37
32D3T10R50L	-0.0248	2.36
32D3T10R100L	-0.0319	3.04
32D3T20R50L	-0.0691	6.58
32D3T20R100L	-0.0743	7.08

Table 8 Tensile strain distribution (× 10^{-6}).

Specimen type	Load (kN)	10mm	Location	20mm	30mm
32D	20.34	1650	CT5	309	20
32D4T	20.32	1291	CT1	352	33
32D3T	20.39	1263	CT2	30	12
32D4T10R50L	20.16	360	CT7	155	13
32D3T10R50L	20.29	262	CT6	42	9
32D4T10R100L	20.46	176	CT1	110	15
32D3T10R100L	20.39	242	CT6	39	8
32D4T20R50L	20.27	172	CT9	105	17
32D3T20R50L	20.44	60	CT9	13	5
32D4T20R100L	20.22	91	CT9	42	10
32D3T20R100L	20.33	50	CT9	16	3

Table 9 Concrete material parameters (uniaxial compression).

f_c (MPa)	ε_{cl}	E_{ci} (GPa)	E_{cl} (GPa)	E_c (GPa)	k
31.92	0.0023	33.6	16.5	29.7	2.04

Table 10 Concrete material parameters (uniaxial tension).

f_{ct} (MPa)	G_F(N/mm)	w_t (mm)	w_c (mm)
2.98	0.136	0.046	0.229

Table 11 The ultimate load from experiments and finite element analysis.

Specimen ID	$N_{u,Test}$ (kN)	$N_{u,FE}$ (kN)	$N_{u,Test}/N_{u,FE}$
32D	126.97	121.70	1.04
32D4T	166.29	157.36	1.06
32D4T10R50L	183.68	180.62	1.02
32D4T10R100L	185.55	187.28	0.99
32D4T20R50L	195.71	210.64	0.93
32D4T20R100L	232.59	223.10	1.04
		Mean	1.01
		CoV	0.043

Table 12 The ultimate load bearing capacity of models with 32 mm diameter dowel bar (kN).

Thickness (mm) \ Length (mm)	25	50	75	100	125	150
5	166.3	168.2	170.6	172.8	176.7	179.6
10	174.5	180.6	182.2	187.3	192.8	197.6
15	185.3	194.5	197.1	204.1	211.1	217.0
20	196.2	210.6	214.8	223.1	231.4	237.6
25	210.5	226.5	232.8	243.2	252.2	258.5

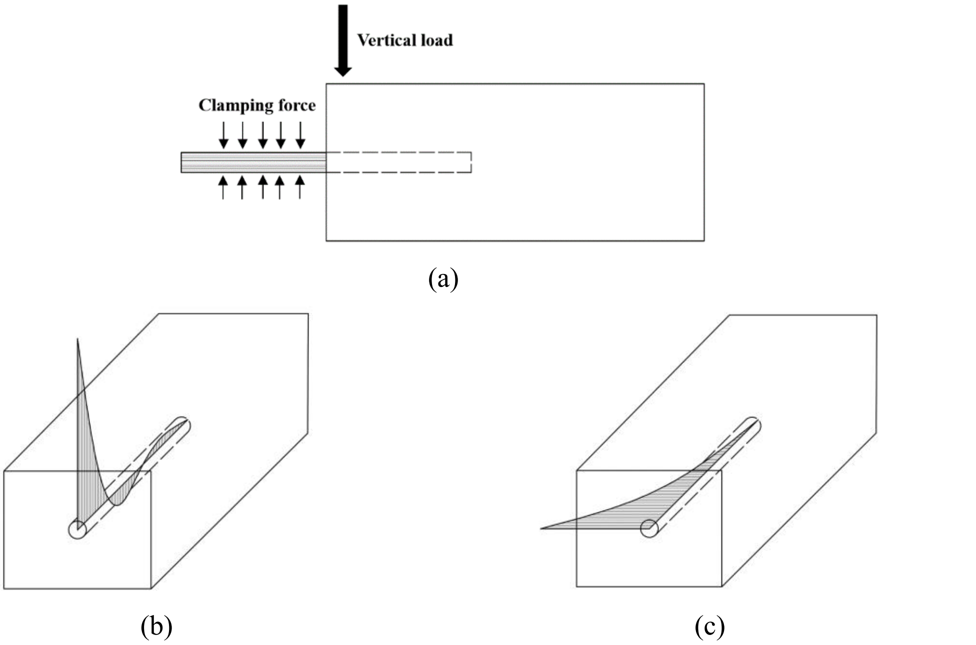

Figure 1. Compressive and tensile stress distributions within dowel slot (a) concrete pavement under vertical load, (b) compressive stress distribution, (c) tensile stress distribution.

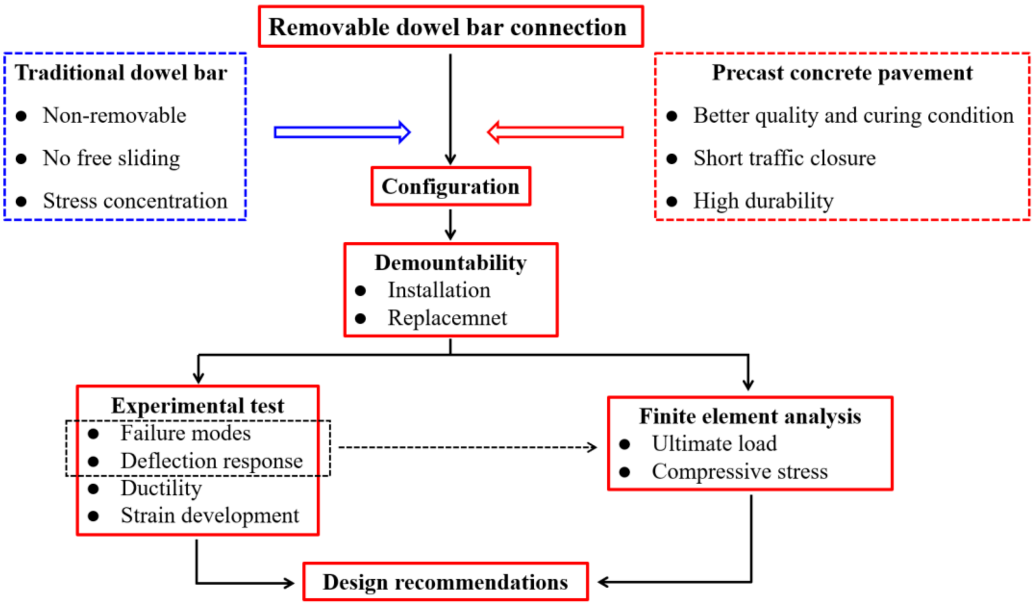

Figure 2. Illustration of research methodology.

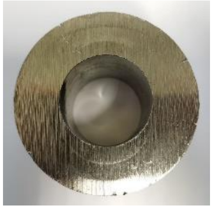

(c)

(d)

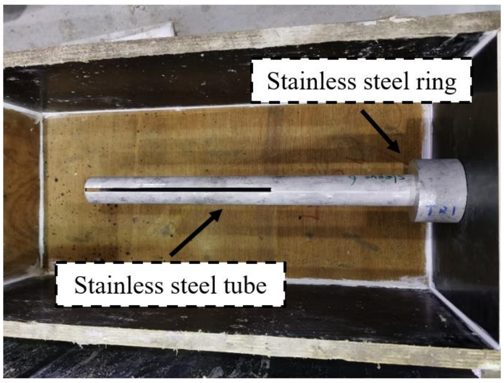

(e)

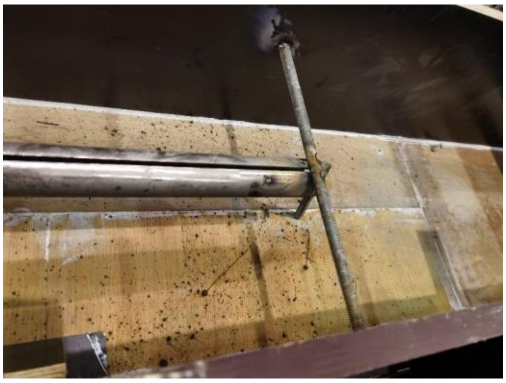

(f)

Figure 3. Constitutions of the removable dowel bar connection system (a) stainless steel dowel bar, (b) stainless steel tube, (c) stainless steel ring with 20 mm thickness, (d) stainless steel ring with 10 mm thickness, (e) assemble stainless tube and ring in formwork, (f) fix stainless steel tube in formwork.

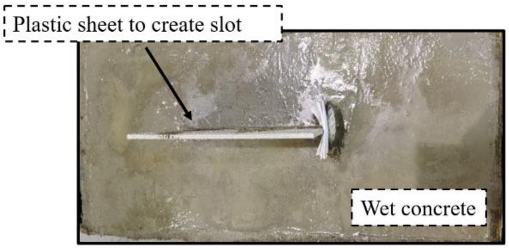

(a)

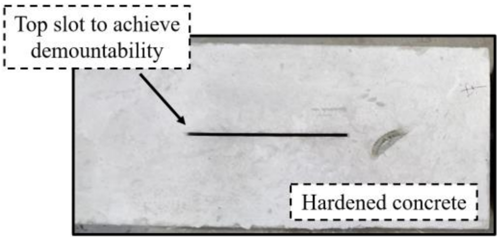

(b)

Figure 4. concrete specimen preparation (a) wet concrete with plastic sheet, (b) hardened concrete with top slot.

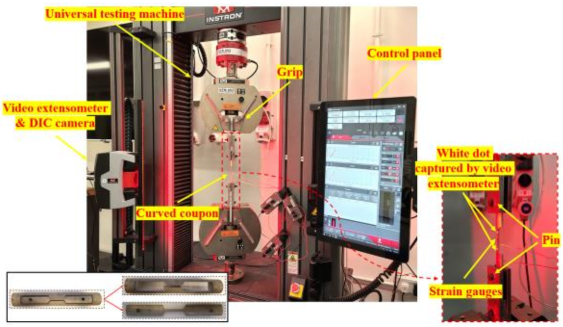

(a)

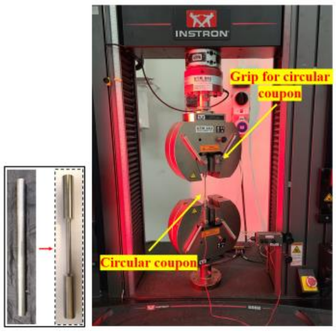

(b)

Figure 5. Tensile material tests of the curved and the circular coupon (a) curved coupon test setup, (b) circular coupon test setup.

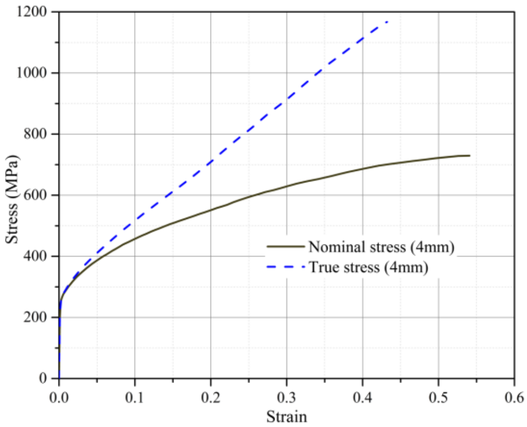

(a)

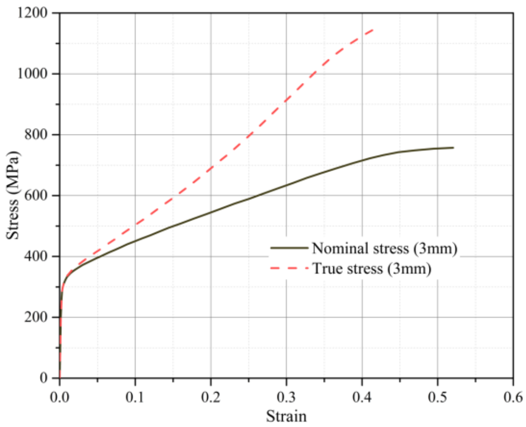

(b)

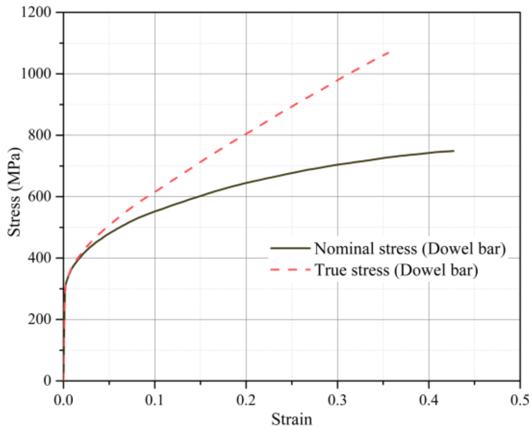

(c)

Figure 6. Typical stress-strain curves of stainless steel (a) 4 mm thick stainless steel tube, (b) 3 mm thick stainless steel tube, (c) stainless steel dowel bar.

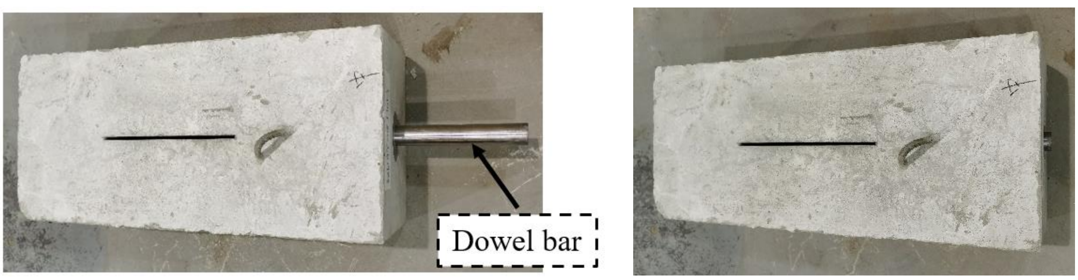

(a)

(b)

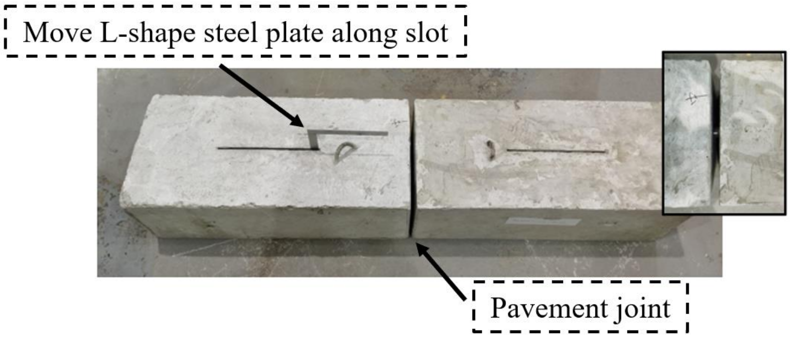

(c)

Figure 7. Removable dowel bar installation procedure (a) insert the dowel bar into an individual pavement slab, (b) push the dowel bar into the adjacent pavement slab and (c) move the dowel bar to the target location.

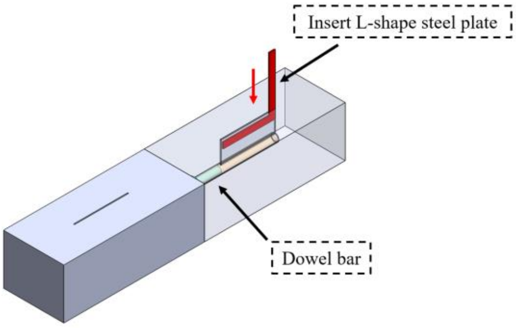

(a)

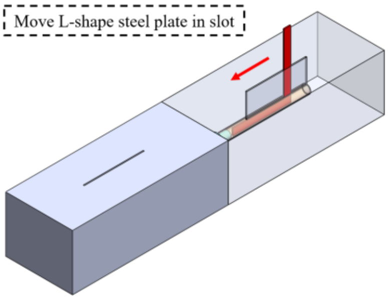

(b)

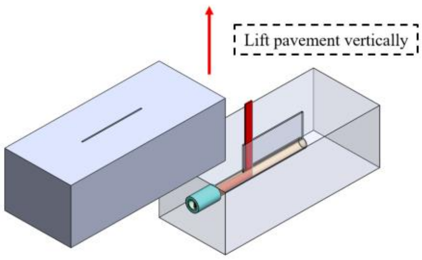

(c)

Figure 8. Removable dowel bar replacement procedure (a) insert L-shape steel plate into the slot, (b) push the dowel bar into the adjacent slab and (c) lift the pavement with the dowel bar vertically.

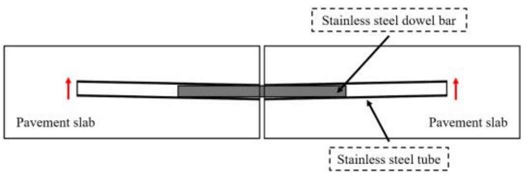

(a)

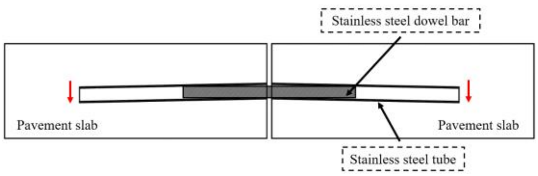

(b)

Figure 9. Stainless steel tube misalignment (a) upward misalignment, (b) downward misalignment.

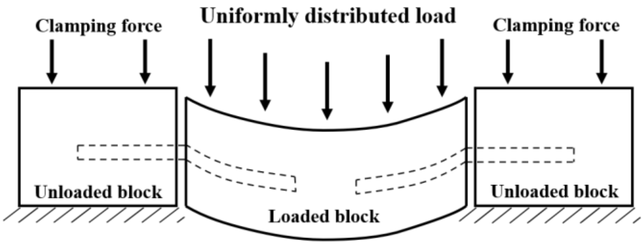

Figure 10. AASHTO T253 test method.

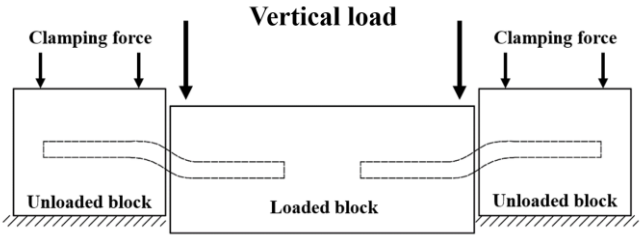

Figure 11. The modified AASHTO T253 test method.

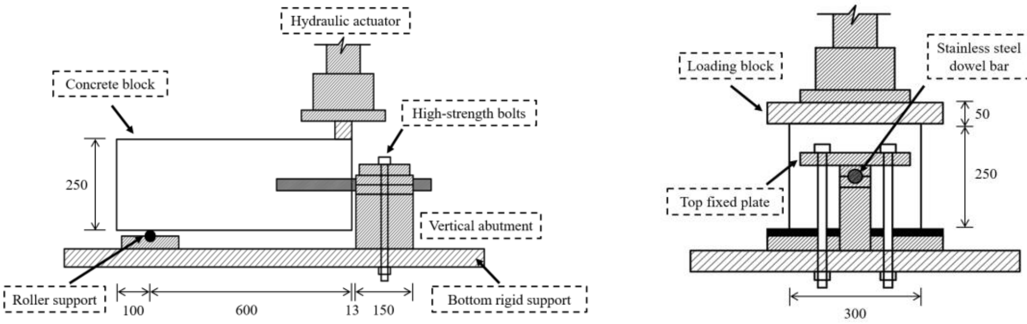

(a) (b)

Figure 12. Schematic diagram of the experimental test setup (a) side view, (b) front view (mm).

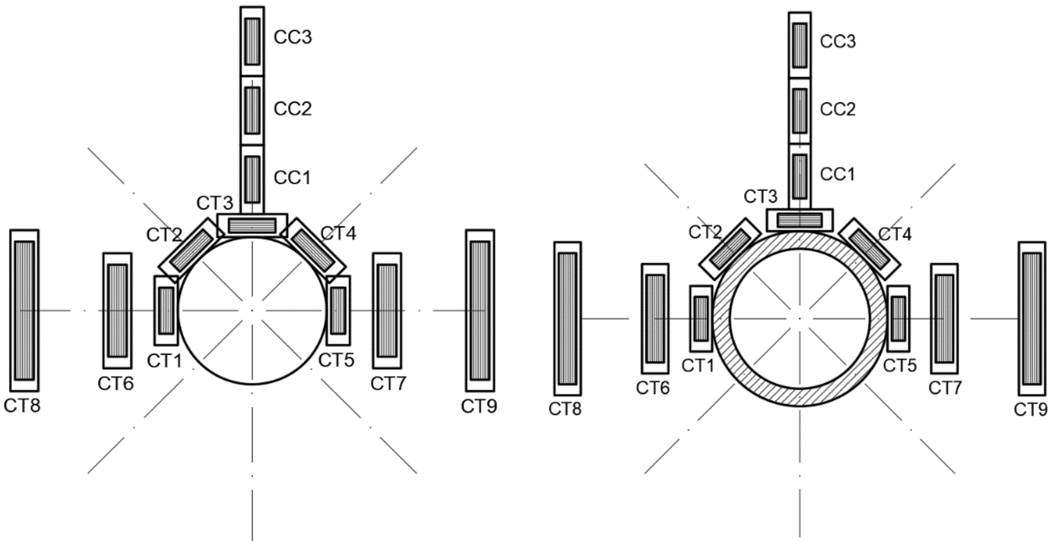

(a) (b)

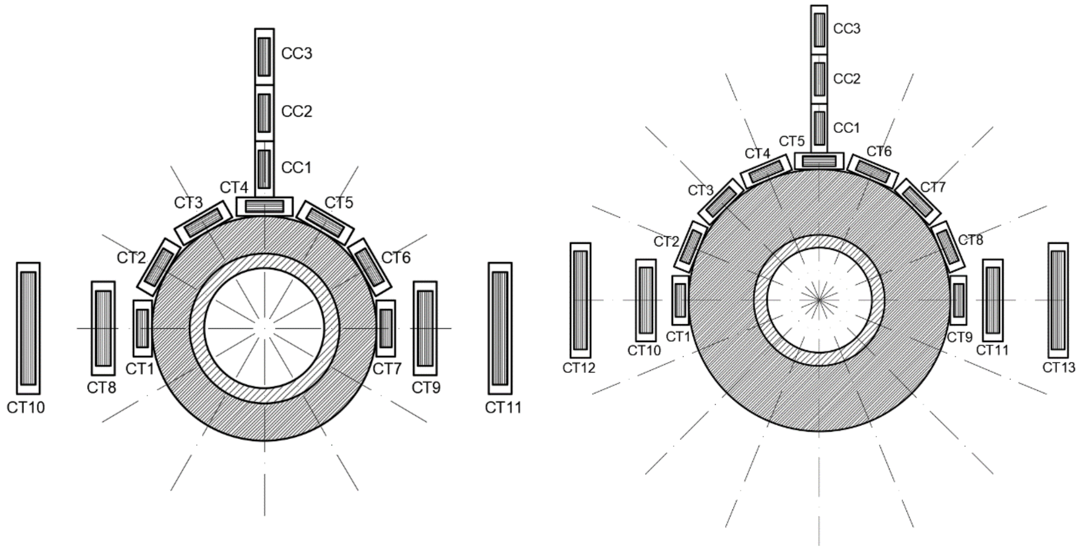

(c) (d)

Figure 13. Strain gauges arrangement in test specimens (a) 32D, (b) 32D4T(3T), (c) 32D4T(3T)10R and (d) 32D4T(3T)20R.

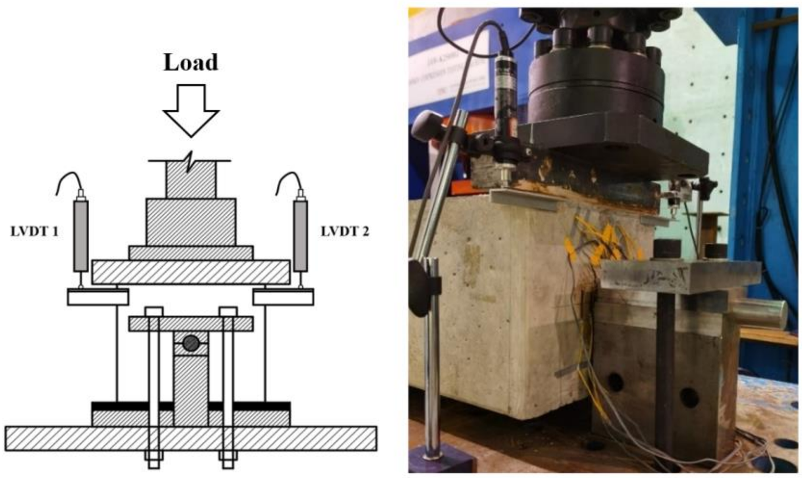

Figure 14. LVDTs arrangement in experiments.

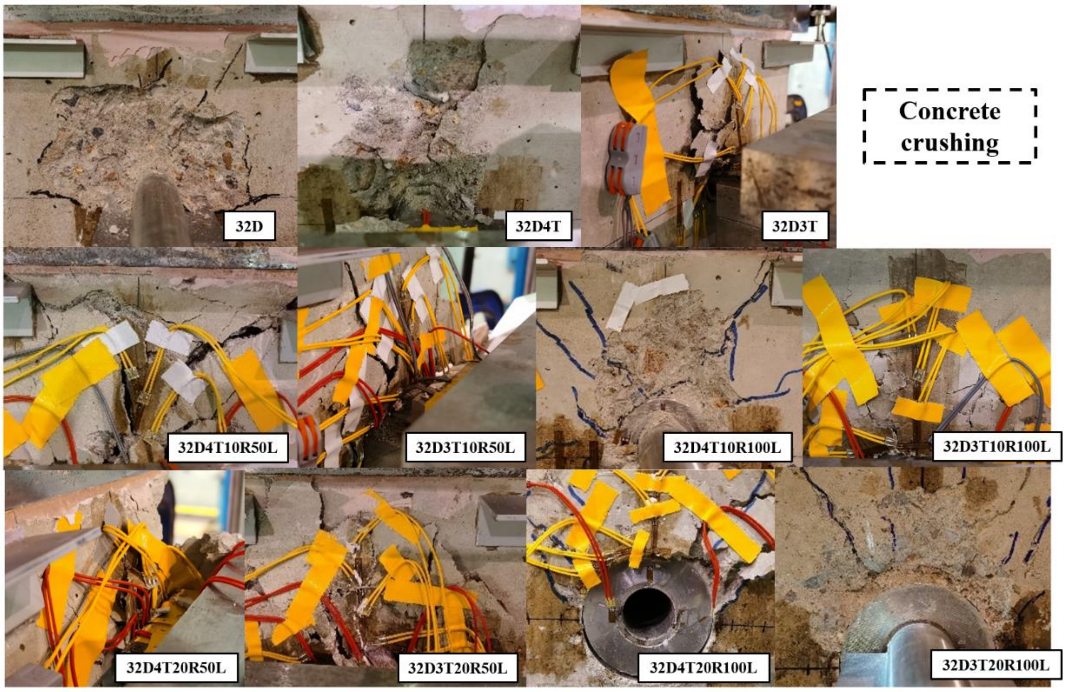

Figure 15. Concrete crushing failure.

(a)

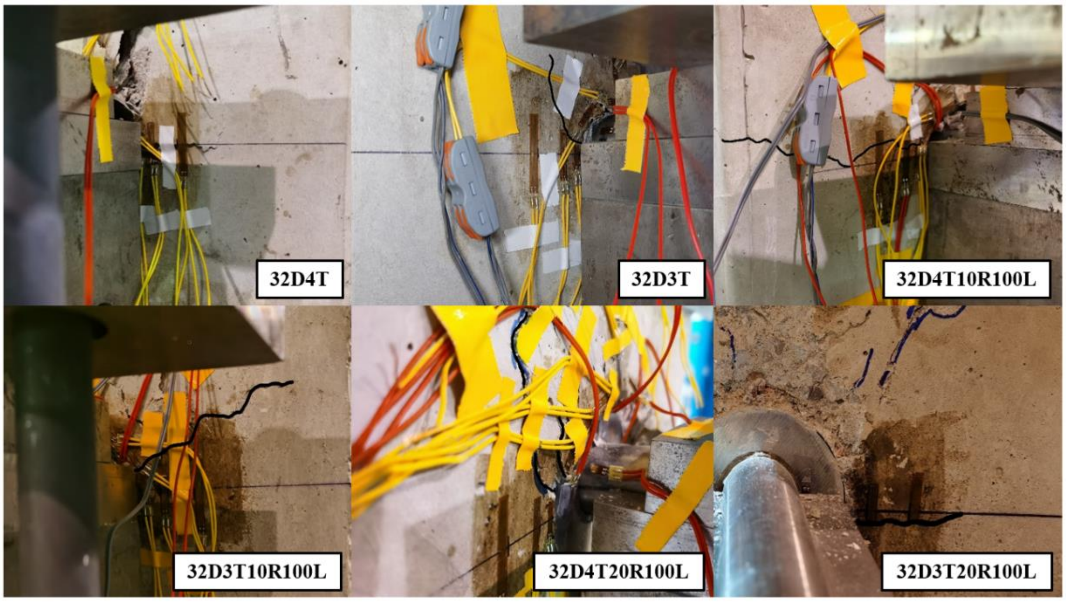

(b)

Figure 16. Concrete tensile cracks (a) horizontal tensile cracks in specimen 32D, (b) horizontal tensile cracks in specimens with the stainless steel tube and the stainless steel ring.

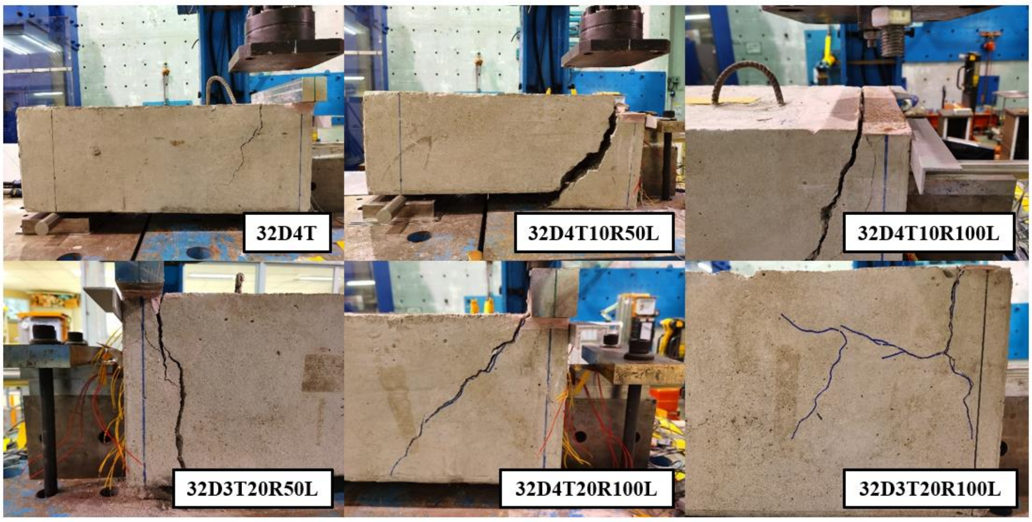

Figure 17. Brittle side shear cracks in concrete blocks after experiments.

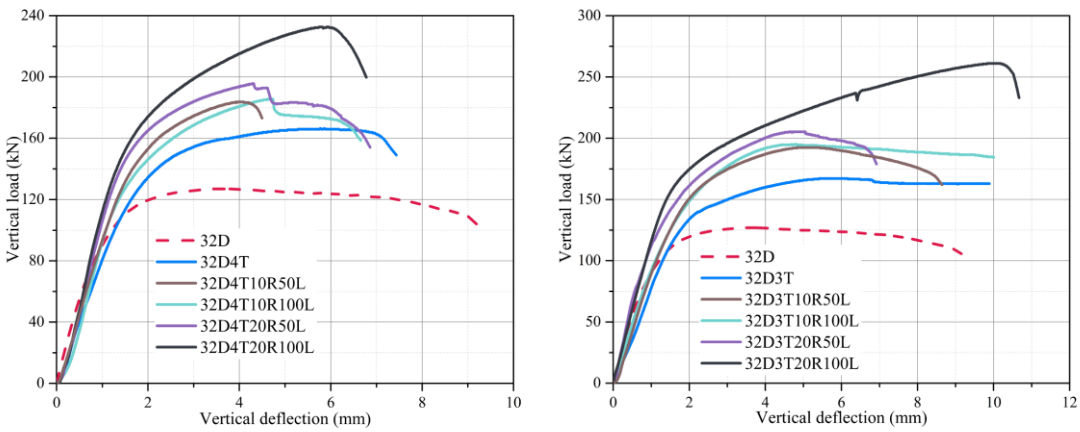

(a) (b)

Figure 18. Load-deflection relationships of test specimens (a) 4T specimens and (b) 3T specimens.

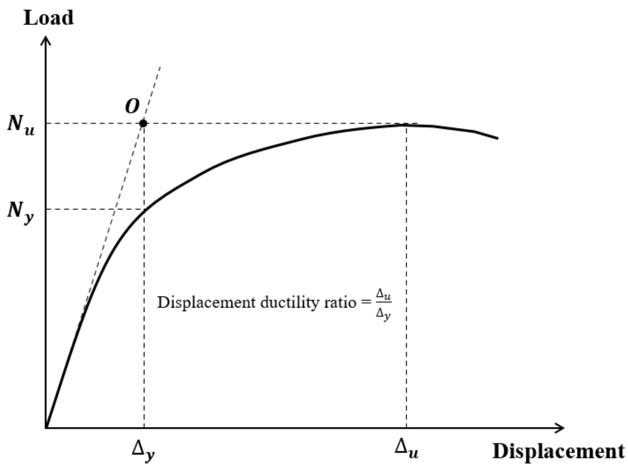

Figure 19. Definition of the dispalcement ductility ratio.

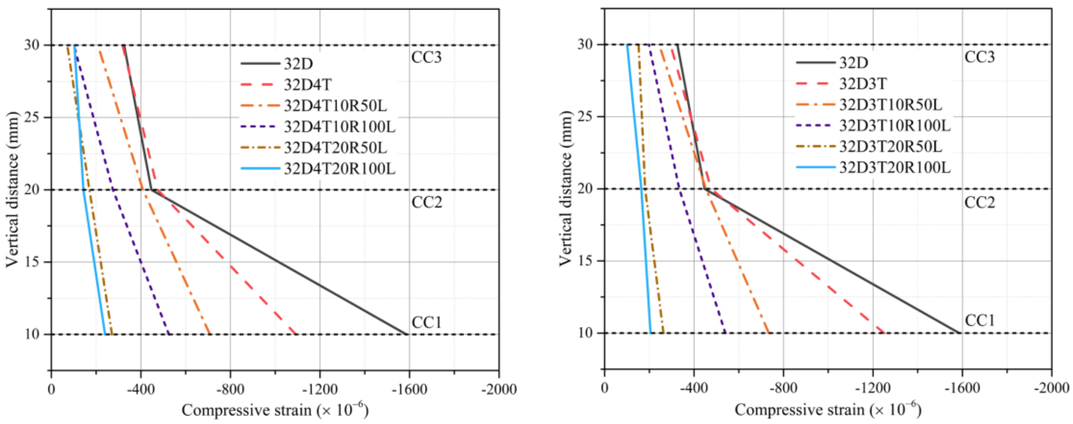

(a) (b)

Figure 20. Concrete compressive strain distribution (a) 4T specimens, (b) 3T specimens.

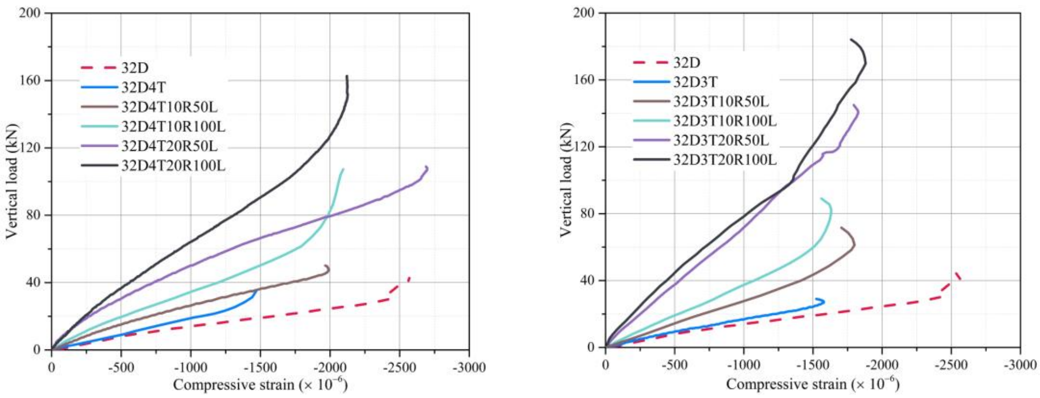

(a) (b)

Figure 21. Compressive strain development in strain gauge CC1 (a) 4T specimens, (b) 3T specimens.

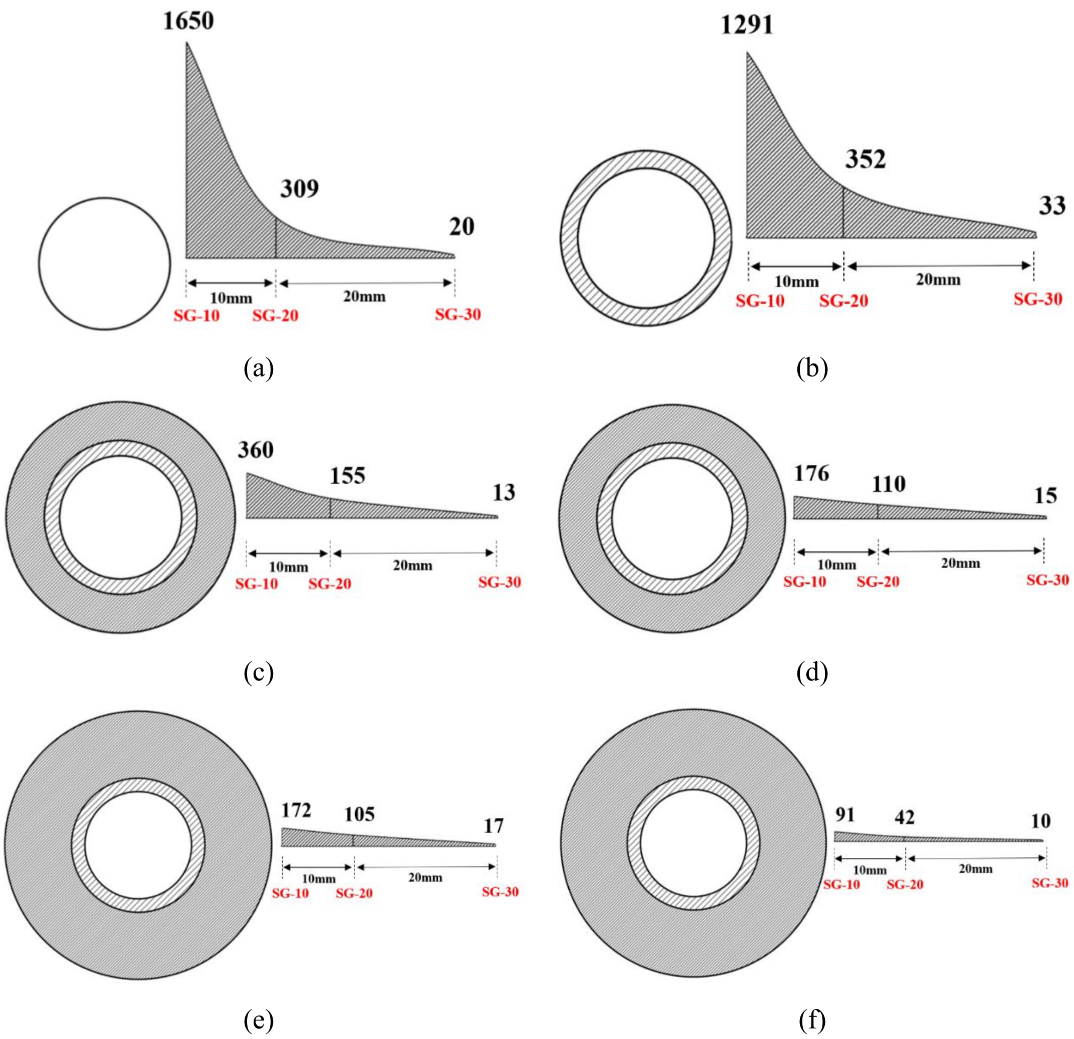

Figure 22. Tensile strain distributions of 4T specimens under 20 kN ($\times 10^{-6}$) (a) 32D, (b) 32D4T, (c) 32D4T10R50L, (d) 32D4T10R100L, (e) 32D4T20R50L, (f) 32D4T20R100L.

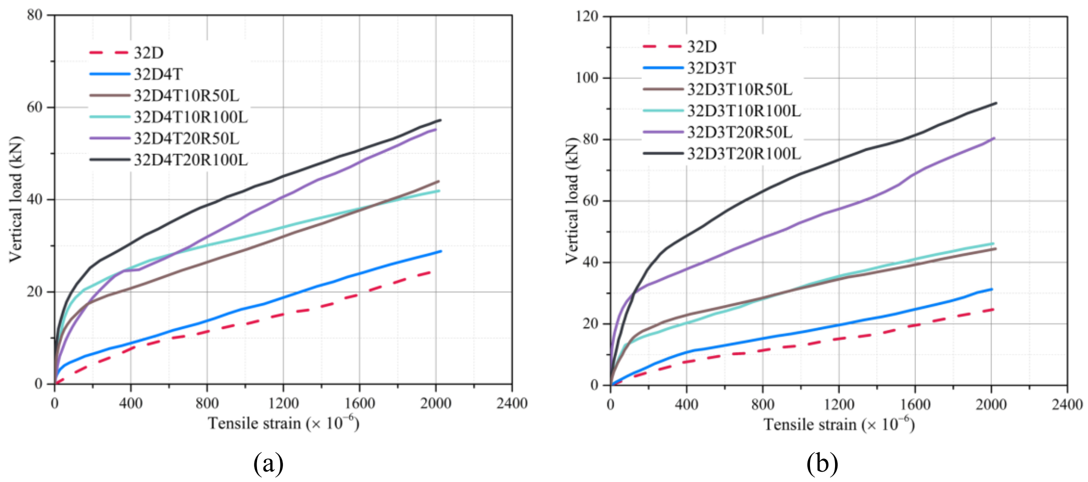

Figure 23. Tensile strain development of 4T and 3T specimens (a) 4T specimens, (b) 3T specimens.

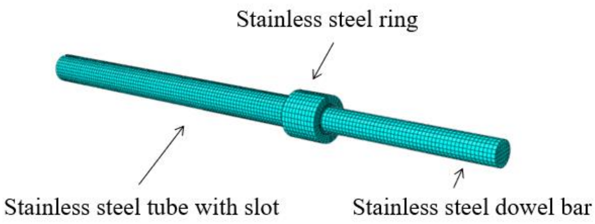

(a)

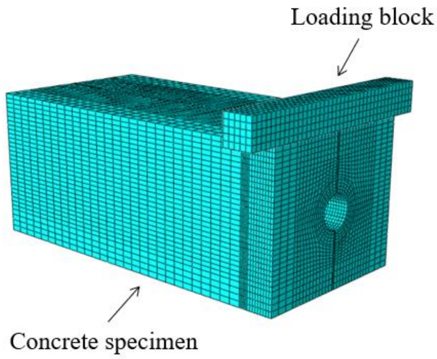

(b)

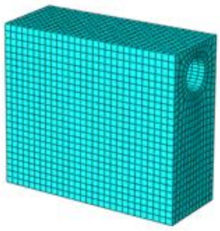

(c)

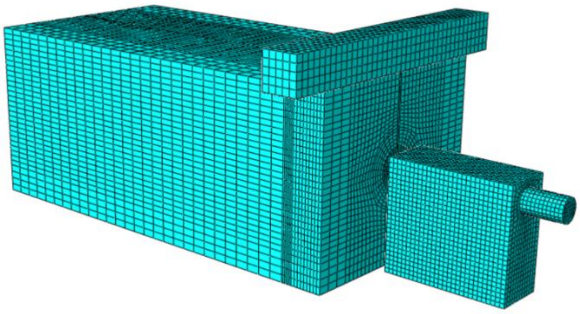

(d)

Figure 24. Finite element model (a) removable dowel bar connection system, (b) concrete specimen and loading block, (c) fixing device and (d) assembled model

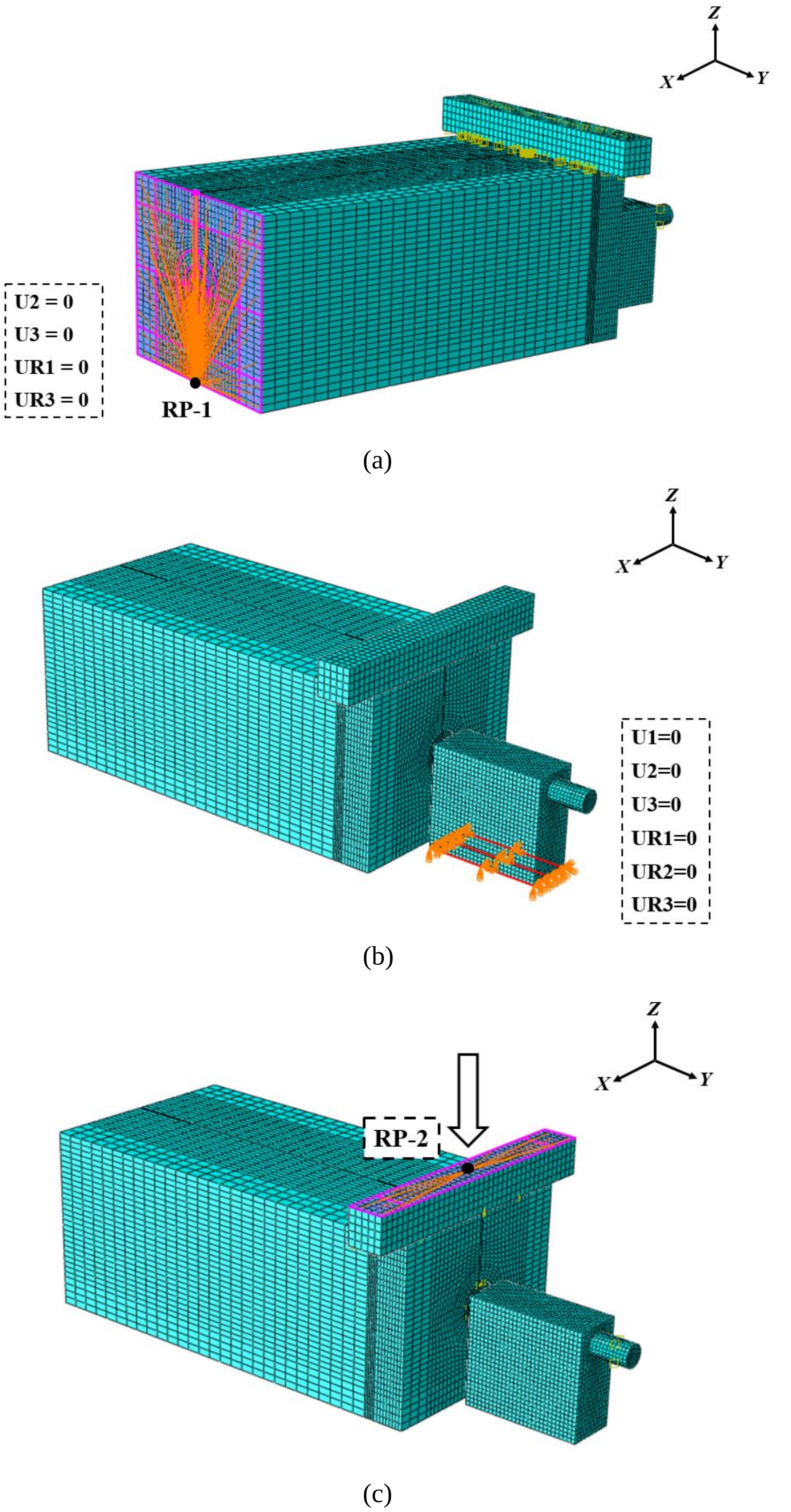

Figure 25. Boundary conditions and loading arrangement in the finite element analysis (a) roller support modelling, (b) boundary conditions of the fixing device and (c) loading arrangement.

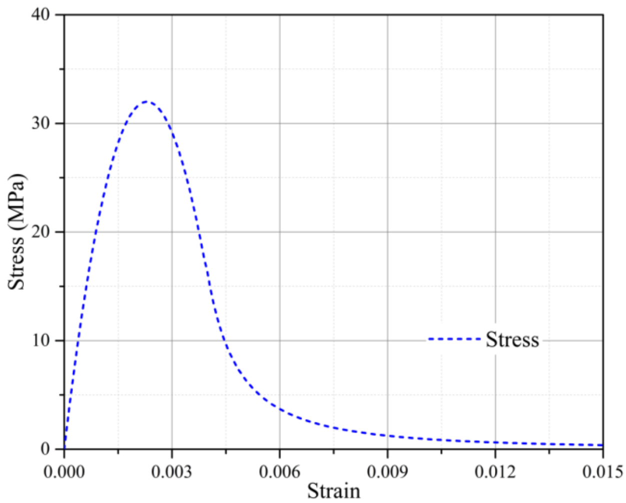

Figure 26. The uniaxial compressive stress-strain curve of concrete.

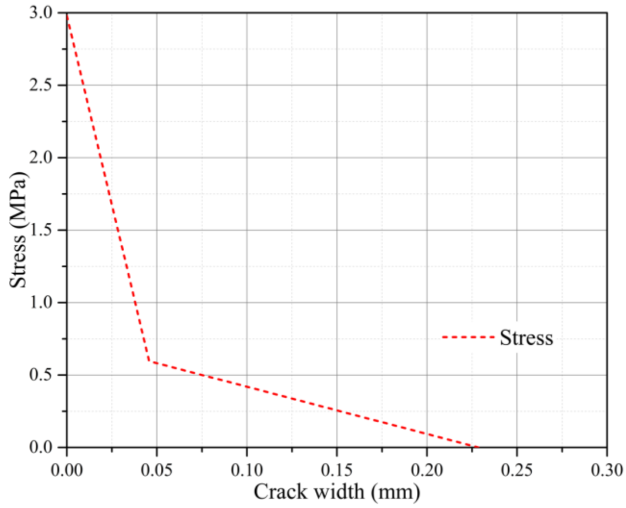

Figure 27. The tensile stress-crack width relationship of concrete.

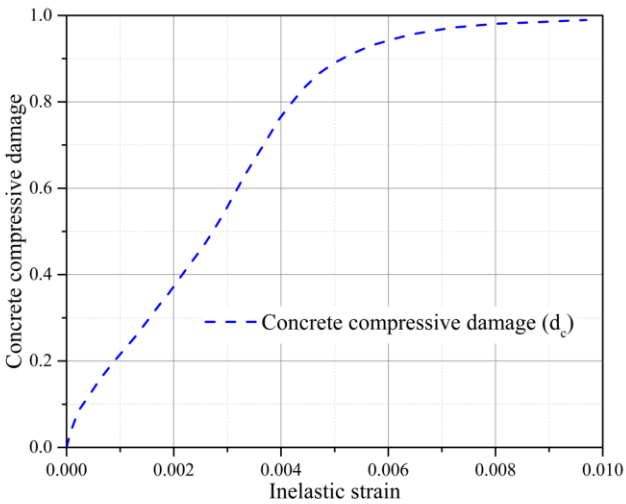

Figure 28. The compressive damage parameter in the finite element analysis.

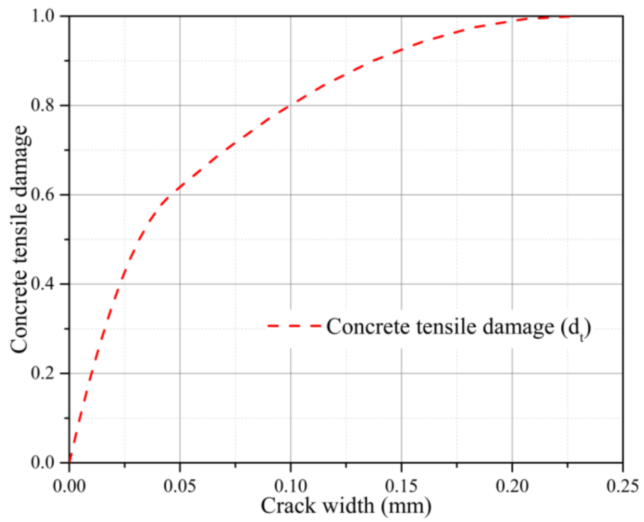

Figure 29. The tensile damage parameter in the finite element analysis.

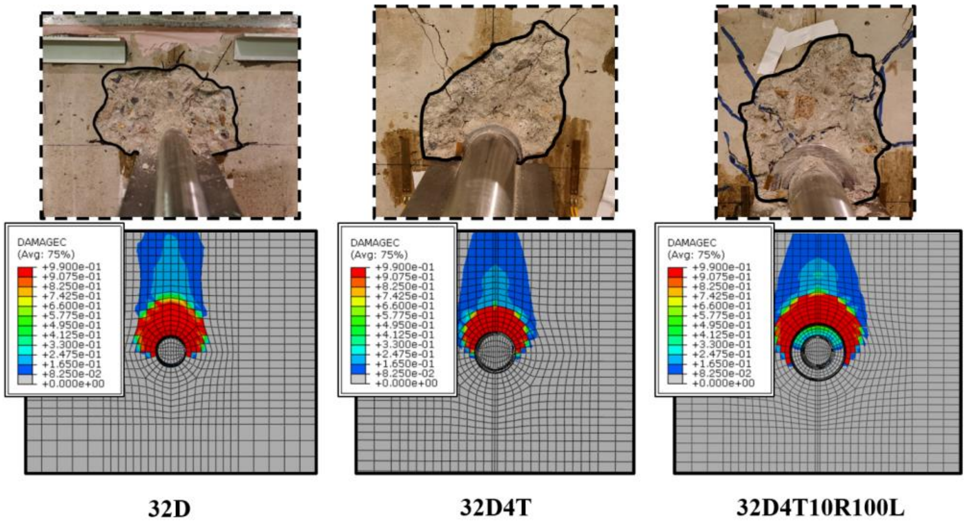

(a)

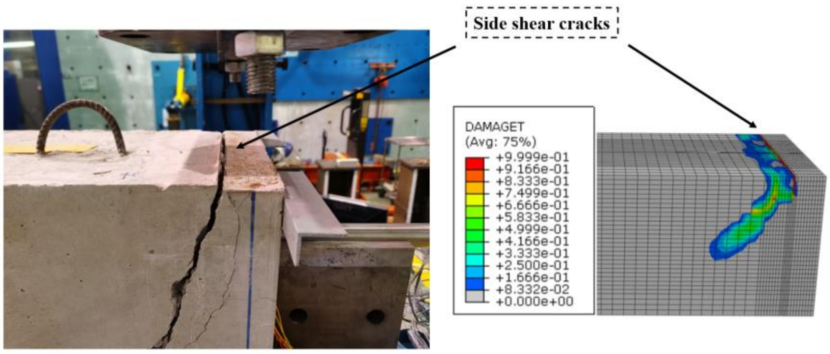

(b)

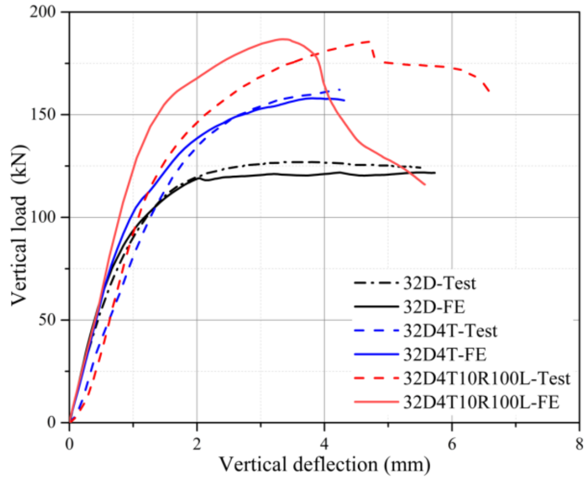

(c)

Figure 30. Model validation (a) concrete crushing, (b) side shear cracks and (c) load-deflection curve.

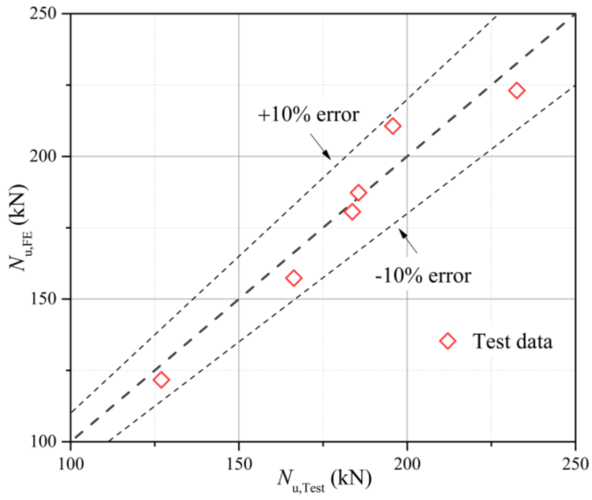

Figure 31. Ultimate load obtained from experiments and predicted in finite element analysis.

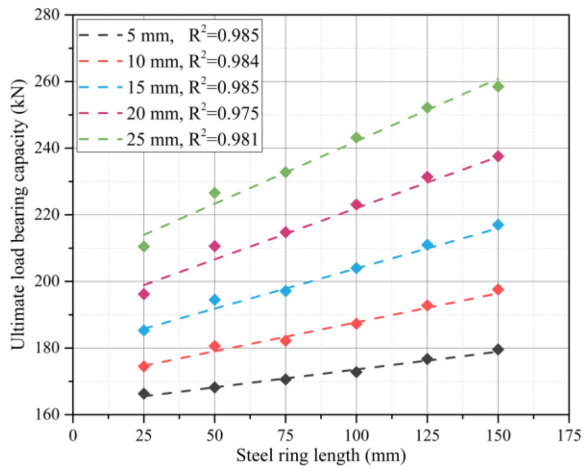

Figure 32. Effect of the stainless steel ring on the ultimate load.

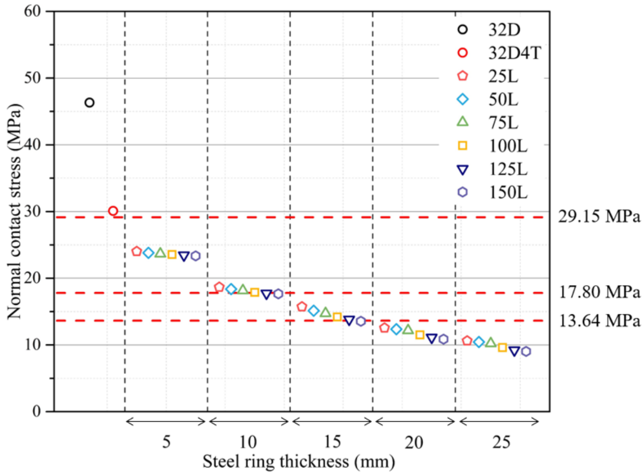

Figure 33. The normal contact stress at the joint surface under 20 kN service load.

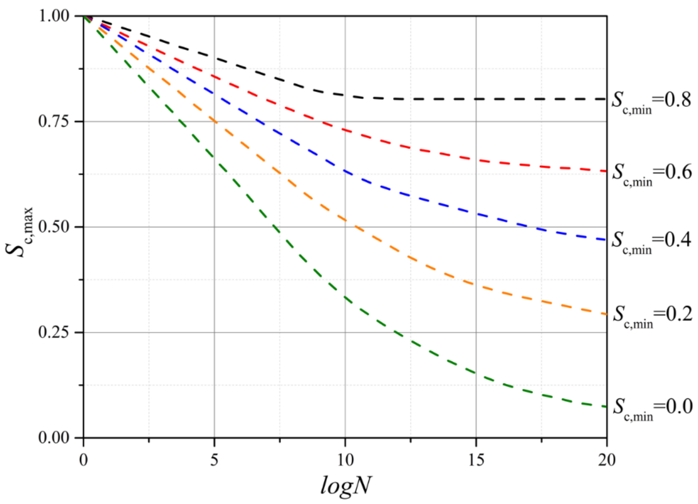

Figure 34. *S-N* curves for concrete under compression.